EES Solar

ROYAL SOCIETY OF CHEMISTRY

MINIREVIEW

View Article Online
View Journal

Check for updates

Cite this: DOI: 10.1039/d5el00218d

Solution processed tandem solar cells for water electrolysis

Hak-Beom Kim, * Woojin Cheon and Tack Ho Lee *

Green hydrogen production *via* solar-driven water splitting stands as a pivotal technology for transitioning to a carbon-neutral economy. While photovoltaic–electrochemical (PV–EC) systems offer a promising pathway by driving water electrolysis as a practical route to solar hydrogen production, single-junction solar cells typically fail to provide the sufficient photovoltage required to drive water electrolysis without external bias. Tandem solar cells, particularly utilizing solution-processable materials, have emerged as a viable solution to overcome this thermodynamic barrier while offering the benefits of low-cost fabrication and mechanical flexibility. This review critically examines recent advancements in solution-processed tandem architectures for unassisted solar water splitting, classifying them into three primary categories: all-organic, all-halide perovskite, and perovskite–organic hybrid tandem systems. We elucidate how bandgap engineering and spectral splitting strategies in these architectures enable high open-circuit voltages (>1.6 V) and improved solar-to-hydrogen efficiencies, reaching up to 17.8%. Beyond material optimization, this article highlights the importance of system-level integration, including the engineering of interconnecting layers, geometric area matching between PV and catalysts, and the development of earth-abundant electrocatalysts for minimizing kinetic overpotentials. Finally, we provide a forward-looking perspective on overcoming critical bottlenecks such as long-term stability in aqueous environments and scalability, aiming to guide future research toward practical and economically viable solar fuel production.

Received 31st December 2025
Accepted 16th April 2026

DOI: 10.1039/d5el00218d

rsc.li/EESSolar

Broader context

The realization of a sustainable hydrogen economy hinges on the ability to produce green hydrogen efficiently and affordably. Solar-driven water splitting represents an ideal solution, yet its widespread adoption is currently hindered by the high fabrication costs and mechanical rigidity of conventional inorganic photovoltaics. This review underscores the transformative potential of solution-processable tandem solar cells, comprising organic and perovskite light absorbers, as a next-generation power source for water electrolysis. By offering a synergistic combination of tunable optoelectronic properties, light weight, and compatibility with high-throughput manufacturing, these materials address the dual challenges of performance and cost. We provide a comprehensive roadmap linking fundamental material innovations with practical system engineering, such as catalyst integration and stability management. This work identifies the critical steps required to transition from laboratory-scale efficiency records to scalable, durable, and cost-competitive solar-to-hydrogen platforms; thereby accelerating the deployment of renewable fuel technologies in the global energy landscape.

1 Introduction

The escalating global climate crisis and the urgent need for energy decarbonization necessitate a profound shift toward sustainable energy carriers. Among various options, green hydrogen, produced *via* renewable energy, has emerged as a cornerstone for achieving a sustainable hydrogen economy.[1,2] Green hydrogen is essential because it offers a clean, high energy density medium for long-term energy storage and a direct replacement for fossil fuels across hard-to-abate sectors like industry and heavy transport.[1,3–6] Among the methods for producing green hydrogen, a representative approach involves water splitting utilizing solar energy. This method directly converts the most abundant renewable energy source, solar energy, into a chemical fuel. The conversion of solar energy into hydrogen is primarily realized through the integration of a photovoltaic (PV) device and an electrochemical (EC) cell, known as the PV–EC system. For water electrolysis, single-junction solar cells are fundamentally limited by the Shockley–Queisser efficiency threshold,[7,8] and consequently suffer from insufficient photovoltage output to drive the reaction, motivating increasing interest in tandem architectures,[7,9] where subcells with complementary bandgaps are connected in series to deliver enhanced photovoltage and overall conversion efficiency. In 2016, a notable milestone was achieved with the

Department of Chemistry Education, Graduate Department of Chemical Materials, Institute for Plastic Information and Energy Materials, Sustainable Utilization of Photovoltaic Energy Research Center, Pusan National University, Busan 46241, Republic of Korea. E-mail: hbkim@pusan.ac.kr; tackho@pusan.ac.kr

report of over 30% solar-to-hydrogen (STH) conversion efficiency using a triple-junction InGaP/GaAs/GaInNAsSb solar cell, underscoring the potential of tandem devices for solar fuel production.[10]

However, despite their high efficiencies, incumbent tandem technologies face major challenges, including high fabrication costs, material scarcity, and mechanical rigidity, which limit their suitability for large-scale deployment.[11–14] These limitations have spurred increasing interest in solution-processable semiconductors, particularly organic and metal halide perovskite light absorbers. Both classes of materials offer important advantages, such as low-cost fabrication, facile bandgap tunability, and compatibility with flexible substrates, making them attractive for the design of tandem solar cells with distinctive manufacturing and mechanical benefits.[15–20] Tandem solar cells composed of organic and/or perovskite subcells have therefore emerged as promising candidates for next-generation PV technologies, particularly in applications requiring high photovoltage, lightweight structures, and mechanical flexibility.[21,22] Nonetheless, these emerging solution-processable tandems face their own significant hurdles that must be overcome for practical deployment. Key challenges include intrinsic material instability, particularly the notorious sensitivity of perovskites to moisture and oxygen, and the photodegradation of organic absorbers.[23–27] Furthermore, achieving efficient charge recombination at the interconnecting layer, minimizing interfacial voltage losses, and ensuring robust encapsulation for long-term operation in aqueous environments remain critical bottlenecks.

This minireview summarizes recent progress in solution-processed tandem architectures specifically aimed at solar-driven water electrolysis. We categorize the relevant systems into three primary categories: organic, halide perovskite, and perovskite–organic hybrid tandems. By focusing on advances in materials design, interfacial engineering, and system integration strategies for PV–EC configurations, we elucidate the prevailing challenges for each technology. Finally, we provide a forward-looking perspective on the research directions required to enable efficient, durable, and scalable solar-to-hydrogen conversion.

Hak-Beom Kim

Dr Hak-Beom Kim received his B. S. in Ceramic Engineering from Hongik University and PhD in Energy Engineering from Ulsan National Institute of Science and Technology (UNIST) under the supervision of Prof. Jin Young Kim. He is currently a postdoctoral researcher at Pusan National University, South Korea. His research interests include perovskite-based photovoltaic devices, large-area perovskite solar cells, and photoelectrochemical hydrogen production, with expertise in interfacial engineering, thin-film fabrication, and tandem solar cell architectures.

Tack Ho Lee

Tack Ho Lee started his current position of Assistant Professor in the Department of Chemical Materials at Pusan National University from 2023. His research addresses emerging semiconductors for solar energy conversion since the start of his postgraduate at UNIST. After receiving a doctorate in 2020, he has fostered an interest in organic semiconductors from photovoltaics to photoelectrochemical fuel synthesis, and finally in time-resolved spectroscopy after moving to the Durrant group at Imperial College London in 2020 as a Postdoctoral Research Associate. His group now develops photoelectrodes and photocatalysts for solar-driven fuel synthesis from organic and perovskite light absorbers.

2 Water electrolysis and tandem solar cells: solution processable PV materials

2.1 Water electrolysis systems for hydrogen production

The PV–EC system is a modular approach for solar-to-hydrogen conversion, where a PV cell is electrically connected to an EC cell (electrolyser) to drive water electrolysis using sunlight (Fig. 1a). The PV cell in the PV–EC system only needs to provide a sufficient voltage difference across its external terminals, regardless of the absolute potential alignment of its internal bands with the electrolyte. As illustrated in Fig. 1a, the hydrogen evolution reaction (HER) takes place at the hydrogen evolution catalyst (HEC)-loaded cathode, while the oxygen evolution reaction (OER) occurs at the oxygen evolution catalyst (OEC)-loaded anode. In acidic and alkaline media, these half-cell reactions are represented as follows:[28–30]

2.1.1 Cathodic reaction (HER). In acidic electrolyte,

$$2H^+ + 2e^- \rightarrow H_2 \tag{1}$$

In alkaline electrolyte,

$$2H_2O + 2e^- \rightarrow H_2 + 2OH^- \tag{2}$$

2.1.2 Anodic reaction (OER). In acidic electrolyte,

$$2H_2O \rightarrow O_2 + 4H^+ + 4e^- \tag{3}$$

In alkaline electrolyte,

$$4OH^- \rightarrow O_2 + 2H_2O + 4e^- \tag{4}$$

The overall water electrolysis reaction can be expressed as:

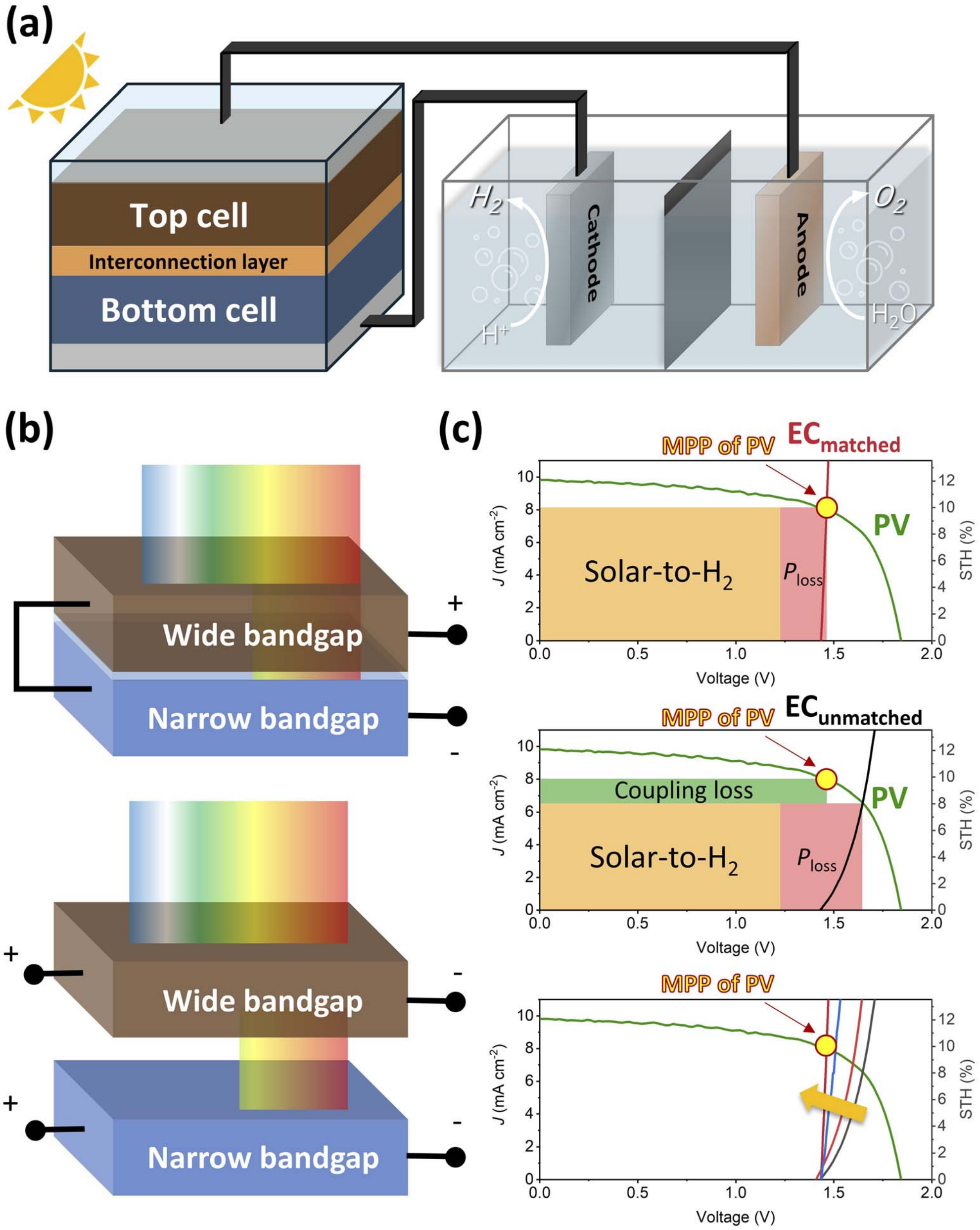

Fig. 1 (a) Schematic illustration of a PV–EC water electrolysis system. (b) Tandem solar cell configurations: two-terminal (top) and four-terminal (bottom). (c) *J*–*V* characteristics of tandem PV (green) and EC in a two-electrode configuration. The MPP of PV is marked with a yellow circle and the operating point of EC is defined as the point where the *J*–*V* curves of OPV and EC intersect. The amount of power stored as hydrogen (Solar-to-H_2) and that wasted as kinetic loss (P_{loss}) are indicated. The coupling loss is generated (green box), when the MPP of PV and the operating point of EC is not matched. Adjusting this operating point to coincide with the MPP of PV (yellow arrow at the bottom) allows the generated power to be fully transferred to EC with a minimal loss.

$$2H_2O \rightarrow 2H_2 + O_2 \tag{5}$$

The Gibbs free energy required to split water under standard conditions (25 °C, 1 atm) is 237.2 kJ mol^{-1}, corresponding to a thermodynamic potential of 1.23 V. However, in practical systems, the applied voltage must exceed the thermodynamic limit of 1.23 V owing to kinetic constraints, often requiring 1.6–2.0 V for sustained water electrolysis.[31] This increase in required voltage under non-ideal conditions can be explained using the Nernst equation.

2.2 Voltage requirements and detailed-balance rationale for tandem operation

Unassisted water electrolysis requires not only the thermodynamic minimum voltage of 1.23 V but also an additional potential to overcome catalytic overpotentials and resistive losses. As a result, a high photovoltage of approximately 1.8 V or higher is required for practical operation.[32,33] Under these conditions, a single-junction photoabsorber inevitably faces a fundamental trade-off between photocurrent generation and photovoltage output. Specifically, a narrow bandgap is advantageous for achieving high photocurrent, whereas a wide bandgap is necessary to provide sufficient voltage for unassisted water splitting.[34,35] From the perspective of the detailed-balance or Shockley–Queisser limit, this trade-off imposes a strict upper bound on the efficiency of single-absorber systems and provides a fundamental rationale for tandem architectures. By enabling broader utilization of the solar spectrum, tandem configurations serve as an essential design strategy to simultaneously achieve high photocurrent and high photovoltage.[36,37]

When intrinsic optical limitations such as thermalization and transmission losses are considered together with practical operational losses including overpotential and power mismatch, the STH conversion efficiency of single-junction PV–EC systems is theoretically limited to about 20%. The tandem structure, proposed as a means to overcome this limitation, can improve the practical efficiency to around 30%, and theoretical studies predict efficiencies exceeding 40%.[9,10] In particular, solution-processed perovskite and organic absorbers have recently attracted considerable attention, although their intrinsically low photovoltage for unassisted water electrolysis restricts STH efficiency in single-junction systems to below 10–15%. However, the incorporation of perovskite-based tandem configurations can increase the practical STH efficiency to approximately 18–20%, and further bandgap optimization is expected to yield theoretical efficiencies approaching 30%.[38,39]

The essential significance of tandem architectures is that it enables the voltage required for unassisted water splitting to be achieved without excessive photocurrent loss. Therefore, the distinction between two-terminal (2T) and four-terminal (4T) tandem architectures should be viewed not as a question of whether tandem architecture is necessary, but rather as a matter of how to implement tandem configurations most effectively at both the device and system levels.[40]

2.3 Tandem structures for unassisted water electrolysis

In light of the foregoing discussion, the central challenge in unassisted PV–EC water electrolysis lies not in whether tandem architectures are necessary, but rather in how tandem functionality can be most effectively realized at both the device and system levels. By incorporating two photoabsorbers with complementary bandgaps, tandem photovoltaic configurations provide a viable pathway toward satisfying the photovoltage requirement for bias-free water splitting while maintaining efficient utilization of the solar spectrum.[41] Depending on the mode of electrical interconnection between the top and bottom subcells, tandem devices are broadly categorized into 2T monolithic and 4T architectures (Fig. 1b). These two configurations differ fundamentally in their approaches to voltage generation, current matching, optical management, fabrication complexity, and system integration, and thereby present distinct opportunities and trade-offs for PV–EC water electrolysis systems.

In the 2T configuration, the two subcells are monolithically integrated and electrically connected in series *via* an intermediate recombination layer, such as a tunnel junction or a transparent recombination junction. The overall open-circuit voltage (V_{OC}) approximates the sum of the V_{OC} values generated by each subcell, while the operating current is limited by the subcell producing the lowest photocurrent as a consequence of the series connection. This architecture offers practical advantages in terms of wiring simplicity, ease of current matching, module integration, and direct coupling with electrolyzers. However, 2T tandems are inherently sensitive to current mismatch between subcells; any perturbation of the current balance established under standard test conditions, whether caused by spectral or thermal variations during operation, can lead to significant performance degradation. Moreover, the monolithic stacked structure demands high-quality intermediate recombination layers and strict process compatibility between subcells, while optical absorption and resistive losses at the interconnecting layers can further compromise device performance.[42]

In contrast, in the 4T configuration, the top and bottom subcells operate electrically independent of one another, allowing each subcell to operate closer to its maximum power point (MPP) without the current-matching constraints imposed by a series-connected tandem. Consequently, 4T tandems generally exhibit greater tolerance to spectral variations and offer higher design flexibility in terms of bandgap selection, material combinations, and subcell optimization.[43] However, realizing these advantages requires additional design elements, including transparent electrodes, individual electrical contacts, and, in many cases, external power management circuitry to combine the outputs of the two subcells.[44] These requirements introduce additional optical interfaces, parasitic absorption, resistive losses, and increased system complexity. Thus, the 2T configuration is advantageous when compact integration and simple direct coupling are prioritized, whereas the 4T configuration is more suitable when high design flexibility and stable operation under variable illumination conditions are required.[40]

Despite this, from the perspective of practical unassisted solar hydrogen production systems, the 2T configuration is often regarded as more significant than the 4T architecture. This is because a 2T tandem integrates two subcells into a single high-voltage photovoltaic unit, thereby enabling direct coupling with an electrolyzer without the need for complex power management circuitry, while also reducing wiring connections, contact interfaces, packaging complexity, and system-level losses.[38] In this regard, although the 4T architecture provides a versatile platform for material exploration and performance optimization, the 2T configuration is more closely aligned with practical device implementation, large-area fabrication, and stack-matched series scaling. In such a configuration, scalability is achieved not by increasing the PV voltage alone, but by proportionally extending both the PV module voltage and the electrolyzer stack voltage through series interconnection, thereby preserving direct voltage-matched coupling across scales without additional power conversion electronics.[45] Furthermore, the 2T architecture is highly compatible with the monolithic integration and series-connected module fabrication technologies established in the conventional photovoltaic industry, which offer important advantages for the scalable deployment of low-cost, high-reliability hydrogen production systems. For these reasons, a growing body of research has focused on 2T tandems, driven not only by the pursuit of high photovoltage, but also by the simplicity, integrability, module compatibility, and potential for balance-of-system cost reduction required for practical applications.[46]

The key challenge for future research therefore lies not simply in achieving a high V_{OC}, but in realizing a 2T tandem architecture capable of simultaneously delivering sufficient current density and long-term stability at the actual water electrolysis operating point. To this end, several critical requirements must be addressed. First, the bandgaps and thicknesses of the top and bottom subcells must be optimized with due consideration of the actual operating spectrum, so as to minimize current mismatch losses under diverse outdoor conditions. Second, optical absorption and resistive losses in the tunnel junction or recombination layer must be mitigated to minimize voltage and fill factor losses arising from series integration. Third, device design should be guided by the actual water-splitting operating point from a holistic PV–EC coupling perspective that encompasses not only the photovoltaic efficiency but also the performance of the catalyst and electrolyzer. Fourth, particularly in the case of perovskite-based tandems, long-term durability and encapsulation stability under photo-, thermal-, moisture-, and electrochemical stress must be ensured, as these represent essential prerequisites for practical deployment. Finally, rigorous engineering validation is required that extends beyond the pursuit of record device efficiencies at the laboratory scale to encompass large-area module fabrication, manufacturing yield, process reproducibility, system cost, and the ultimate levelized cost of hydrogen production.[47]

2.4 PV–EC integration from the standalone systems

The precise synchronization of PV and EC should be considered for efficient solar fuel production from their integration. The operating point of PV–EC is determined by the graphical intersection of the photovoltaic and the electrochemical J–V curve, representing the specific voltage and current at which the PV supply matches the demand of the electrolyzer (Fig. 1c).[48] Single-junction organic and perovskite PVs are now recorded an efficiency of 20%,[49] and 27%,[50] respectively. In the case of tandem configurations (to generate photovoltage 1.7–2.1 V for practical water electrolysis), the state-of-art record efficiency is 21.5%, 29.1%, and 26.4% for organic–organic,[51] perovskite–perovskite,[52] and perovskite–organic tandem PVs.[53] However, the PV efficiency is not directly translated into the EC efficiency in the PV–EC configuration, it is because: electrochemical overpotential losses, voltage/operating-point mismatch, and fill factor losses. To minimize energy waste, impedance matching (or coupling efficiency) must be optimized so that this operating point aligns as closely as possible with the maximum power point (MPP) of PV. Thus, unlike grid-connected electrolyzer, minimizing the loss can be achieved through the rational selection of the sub-cells of tandems to provide the necessary potential/and highly active catalysts to induce a steeper J–V or by the geometric matching between the PV active area and the catalyst electrode area. It indicates that coupling PV and EC directly creates a new operating regime, and design rules of optimal PV–EC should be approached in different ways with standalone PV or EC systems.

In grid-connected PV, a MPP tracker (MPPT) continuously forces the cell to operate at the voltage and the current at the MPP (V_{mp} and I_{mp}) regardless of load. The design target of PV therefore shifts from maximising the output power density (P_{max} at the MPP) to matching the operating voltage window of electrolysers across all insolation conditions. In particular, the voltage match is not just at standard test condition (1 sun, AM 1.5 G). The operating voltage under 0.1 sun illumination can drop 100–150 mV from its 1 sun value, because the V_{OC} of PVs shifts logarithmically with the light intensity.[54] If the electrolysis onset voltage is 1.8 V and the tandem V_{OC} at 0.1 sun falls to 1.75 V, the system simply stops operating: solar-to-hydrogen efficiency collapses to zero, not merely decreases. The voltage margin at low insolation, not peak efficiency at/over 1 sun, is often the binding design constraint. The J–V intersection of the high-FF PV with the electrolyser load line sits close to MPP; but the intersection is pulled toward lower current and lower voltage than MPP with the low-FF PV, indicating that the operating point is doubly penalised. In particular to the series connected tandems, the lowest-FF subcell limits the whole device. In addition, high series resistance (R_S) of PVs causes a faster, non-linear drop in current and voltage, pushing the intersection point far below the optimal operating point, rapidly degrading system efficiency. In PV–EC, the cell spends substantial time near V_{OC} by the lower insolation than 1 sun. For perovskite-based tandems specifically, ion migration is field-dependent and accelerated at high forward bias (near V_{OC}).[55] A cell that appears stable under continuous 1 sun MPP illumination (as is standardly measured) can degrade faster in PV–EC cycling. Therefore, stability tests for the PV cell will be more appropriate at the high forward bias for PV–EC qualification, not at the fixed voltage or MPP for grid-tied systems.

Grid electrolysers (such as proton exchange membrane (PEM) electrolysers) are designed for steady DC input (1.8–2.1 V) and high current density (1–3 A cm^{-2}),[10] while the PV–EC electrolysers operate at low current density (~10 mA cm^{-2} or below, set by PV current) and variable power by insolation. If the PV delivers 15 mA cm^{-2} at 1 sun, the electrolyser must be sized to absorb that current (for a 500 mA cm^{-2} PEM design, you need ~33 times more PV area than electrolyser area); thus, PV–EC electrolysers should be designed with a lower nominal current density than grid PEM. While, thanks to the low current density, membrane resistance (ohmic losses) is essentially negligible in PV–EC. However, start-stop cycling (by the insolation) can cause mechanical stress at the catalyst layer/membrane interface in PV–EC electrolysers, leading to delamination.[48]

2.5 Advantages of solution processable PV materials

The primary motivation for shifting to solution-processable semiconductors is to overcome the significant drawbacks of incumbent tandem technologies. While highly efficient, conventional III–V or silicon-based tandems rely on high-cost, energy-intensive fabrication methods such as vacuum deposition and epitaxial growth.[11–14] This leads to high manufacturing costs and creates mechanically rigid devices, limiting their suitability for large-scale, cost-sensitive PV–EC deployment.

Solution-processable PV materials offer a paradigm shift by enabling low-cost fabrication.[56] This advantage stems from their compatibility with low-temperature processing, which reduces the overall energy and capital expenditure of manufacturing. In particular, solution-processable PV materials present a distinct set of practical advantages for integrated PV–EC systems, particularly in terms of device form factor, fabrication accessibility, and deployment versatility. Andrei *et al.* demonstrated that replacing conventional glass substrates and bulk encapsulants with flexible, thin-film alternatives, enabled directly by the low-temperature solution-based deposition of perovskite absorbers onto plastic substrates, reduces device mass to just 30–100 mg cm^{-2}, a 15-fold reduction relative to traditional photoelectrochemical architectures.[57] This dramatic reduction in gravimetric footprint is not merely an aesthetic advantage: it enables emergent device functionalities that rigid systems cannot access, most strikingly the spontaneous flotation of the assembled artificial leaf driven by gas bubbles evolving during operation, which was validated during outdoor testing on open water. The compatibility of solution-processed perovskites with scalable deposition routes, including the roll-to-roll and doctor-blading techniques already established in the organic PV industry, further suggests that lightweight PV–EC devices could be manufactured and deployed at scales and in environments, such as open water surfaces, that avoid direct competition with land use. In this sense, the processability of the light absorber is not a secondary manufacturing consideration but a primary enabler of the deployment paradigm itself.

3 Water electrolysis driven by solution processable tandem PVs

3.1 Organic tandem PV driven water electrolysis systems

The state-of-art organic photovoltaic (OPV) cells have the bulk-heterojunction structure (mixed polymer donor and small molecular acceptor materials) as a photoactive layer. Typically, the magnitude of the V_{OC} loss is determined by the energy offset between donor and acceptor materials for free charge generation in such BHJ devices.[65] Their single junctions therefore are difficult to produce sufficient photovoltage to drive unassisted water electrolysis that thermodynamically requires 1.23 V and practically demands 1.6–2.0 V due to kinetic overpotentials. To overcome this thermodynamic barrier without external bias, stacking multiple photoactive layers in a tandem configuration has been the primary strategy. Organic tandem solar cells offer a unique advantage in this regard: the bandgaps of organic semiconductors can be easily tuned through molecular design, allowing for precise spectral complementarity between subcells. Furthermore, their compatibility with solution processing enables the fabrication of lightweight and flexible hydrogen production devices, distinguishing them from rigid inorganic counterparts.

3.1.1 Multi-junctions to drive water electrolysis. The development of organic tandem architectures for water splitting has evolved from increasing the number of junctions to optimizing the quality of each junction. In a pioneering 2013 study, Esiner *et al.* employed a triple-junction organic solar cell consisting of PF10TBT:PC$_{61}$BM wide bandgap (1.95 eV) and two PDPPTPT:PC$_{61}$BM narrow bandgap (1.53 eV) subcells to achieve a V_{OC} of 2.33 V and STH efficiency of 3.1%.[58] This device architecture (Fig. 2a) introduced the concept of spectral splitting through bandgap engineering within an all-organic system and demonstrated the feasibility of achieving high voltage output using solution-processable organic materials. A critical enabler for this fully solution-processed stack was the development of a robust intermediate connecting layer comprising ZnO, pH-neutral PEDOT, and Nafion. While the use of conventional acidic PEDOT:PSS typically damages the underlying ZnO layer, substituting it with pH-neutral PEDOT:PSS reduces the work function from 5.05 eV to 4.65 eV, resulting in voltage losses. To address this limitation, the authors adopted a strategy of spin-coating a Nafion solution onto the PEDOT:PSS layer. This specific architecture prevented the acidic corrosion of the underlying ZnO layer during processing and minimized voltage losses, ensuring efficient charge recombination between subcells (Fig. 2b). When the triple-junction solar cell was coupled with Pt electrodes for water electrolysis, an STH efficiency of 3.1% was achieved (Fig. 2c).

To overcome the voltage limitations of single-junction devices, Esiner *et al.* developed a homo-tandem solar cell utilizing a newly synthesized wide bandgap polymer, PTPTIBDT-OD ($E_g = 2.04$ eV), which is intrinsically capable of delivering high V_{OC}.[60] However, realizing the full potential of such high-voltage tandem devices requires precise engineering of the interconnection layer. Fig. 2d illustrates the specific device architecture employed to address this challenge. A conventional interconnection layer based on ZnO and pH-neutral PEDOT:PSS often suffers from a work function mismatch; the low work function of pH-neutral PEDOT:PSS (4.65 eV) creates a non-ohmic contact with deep-HOMO polymers, leading to significant voltage losses. To mitigate this, the authors introduced a thin layer of molybdenum oxide (MoO$_x$) on top of the pH-neutral PEDOT:PSS layer. This MoO$_x$ layer, with its high work function (5.40 eV), serves as an efficient hole collector, ensuring ohmic contact and preventing potential losses at the recombination interface. The impact of this interfacial modification on photovoltaic performance is evident in the *J–V* characteristics shown in Fig. 2e. The control tandem device without any modification exhibited a limited V_{OC} of 1.53 V, confirming the severity of the interfacial barrier. While the incorporation of a Nafion layer resulted in a marginal improvement to 1.58 V, the introduction of the thermally evaporated MoO$_x$ layer dramatically boosted the V_{OC} to 1.74 V. This optimized interconnection layer configuration not only maximized the voltage output but also maintained a high FF of 0.73, which is critical for minimizing power losses during operation. The robust performance of this high-voltage tandem

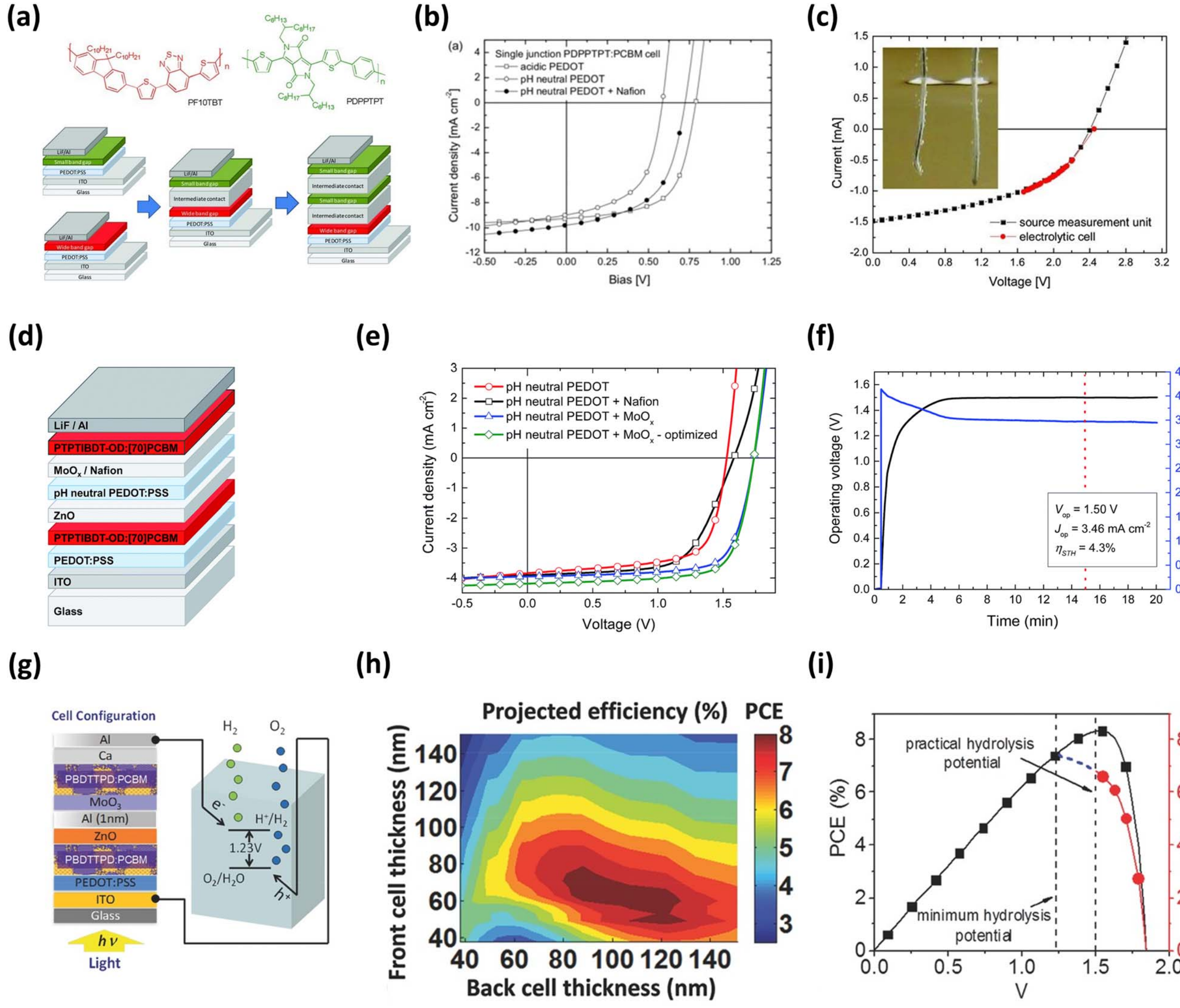

Fig. 2 (a) Molecular structures of the wide bandgap (PF10TBT, $E_g = 1.95$ eV) and narrow bandgap (PDPPTPT, $E_g = 1.53$ eV) polymers (top), and layouts of the single, tandem, and 1 + 2 type triple junction solar cells (bottom). (b) Effect of pH-neutral PEDOT and Nafion on the *J*–*V* curves of single junction PDPPTPT:PCBM solar cells. (c) Comparison of the *I*–*V* curves of the triple junction cell measured using a water electrolysis cell with different sized contacts and using a source-measurement unit. Adapted with permission.[58] Copyright 2013, Wiley-VCH GmbH. (d) Layout of the PTPTIBDT-OD:PCBM homo-tandem solar cell with Nafion or MoO_3 layers in the intermediate contact. (e) Comparison of the *J*–*V* characteristics of PTPTIBDT-OD:PCBM homo-tandem solar cells with and without Nafion or MoO_3 layers in the intermediate contact. (f) Simultaneous measurement of the operating voltage and current density of the device during light-driven electrochemical water splitting using RuO_2 catalysts in 1.0 M KOH. Adapted with permission.[60] Copyright 2016, The Royal Society of Chemistry. (g) Schematic PV-driven electrochemical water splitting study. (h) PCE of homo-tandem solar cells predicted from optical and electrical modelling. (i) PCE of the homo-tandem solar cells (measured *via* source-measurement unit) and estimated STH conversion efficiency (denoted as *η*) at various operating voltages. Adapted with permission.[62] Copyright 2016, WILEY-VCH Verlag GmbH.

cell enabled efficient bias-free water splitting when coupled with RuO_2 electrocatalysts. Fig. 2f displays the simultaneous measurement of the operating voltage and current density of the integrated system over time. The device exhibited stable operation with a stabilized operating voltage (V_{OP}) of 1.50 V, which remarkably aligns with the voltage at the maximum power point ($V_{MPP} \approx 1.48$ V) of the tandem PV. This precise matching between the photovoltaic power output and the electrochemical load resulted in a STH conversion efficiency of 4.3%, demonstrating that interface engineering is a decisive factor in constructing high-efficiency, unassisted solar water splitting systems.

To address the limited photovoltage of single-junction organic solar cells and achieve efficient unassisted water splitting, Gao *et al.* proposed a homo-tandem organic solar cell architecture utilizing a wide-bandgap polymer. Fig. 2g illustrates the schematic of this integrated PV-driven electrochemical water splitting system. The device connects two identical PBDTTPD:$PC_{71}BM$ photoactive layers in series to generate sufficient voltage to overcome the thermodynamic potential of water splitting and kinetic overpotentials. A key enabling feature of this architecture is the robust interconnection layer composed of solution-processed ZnO, ultrathin Al, and MoO_3, which facilitates efficient charge recombination between the subcells while minimizing voltage losses. In a homo-tandem configuration where subcells share identical absorption profiles, balancing the photocurrents is critical for maximizing device performance. To optimize this current matching, the authors employed combined optical and electrical modelling to predict the power conversion efficiency (PCE) as a function of subcell thicknesses. Fig. 2h presents the simulation results, identifying that a specific asymmetric thickness combination—a thinner front cell (60–80 nm) and a thicker back cell (90–130 nm)—is required to achieve PCEs exceeding 8.0%. This configuration ensures that sufficient light

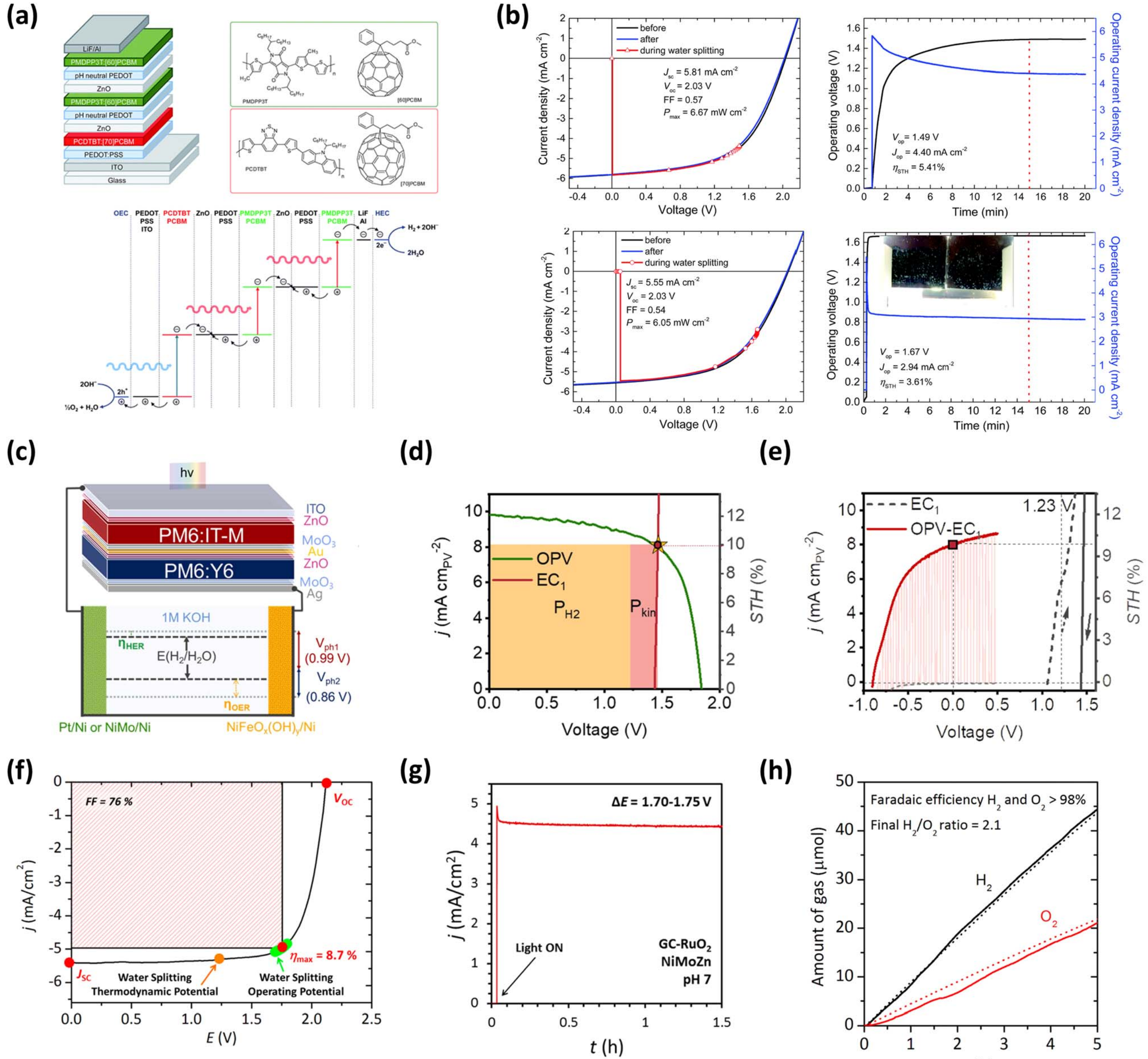

Fig. 3 (a) Device layout of triple junction organic solar cell. (b) *J–V* curves of triple junction solar cells before, during, and after water splitting measurement of 20 min. Adapted with permission.[59] Copyright 2015, The Royal Society of Chemistry (c) schematics of the PM6:IT-M/PM6:Y6 tandem PV–EC system. (d) *J–V* curves of tandem OPV (0.56 cm^2) and EC_1 in a two-electrode configuration (2.0 cm^2). The MPP of PV and the operating point of EC_1 are marked with a star and a dot, respectively. The amount of power stored as hydrogen (P_{H_2}) and that wasted as kinetic loss (P_{kin}) are indicated. (e) LSV of EC_1 in a two-electrode configuration and OPV–EC system with its STH efficiency. Adapted with permission.[63] Copyright 2022, Elsevier B.V (f) *J–V* curve of the triple junction solar cell. (g) Current density *vs.* time profile of a water splitting experiment using a triple junction solar cell (a PCE of the PV was 8.5%), GC-RuO_2 anode, and NiMoZn cathode in a two-electrode configuration and a two-compartment cell containing 0.1 M phosphate buffer, pH = 7.0, under AM 1.5 G illumination with a GG400 filter. (h) Gas evolution of the water splitting experiment using the triple junction solar cell under the same condition. Adopted with permission.[61] Copyright 2016, American Chemical Society.

is transmitted through the front cell to be absorbed by the back cell, effectively balancing the photocurrents despite the identical bandgaps. Guided by this modelling, an optimized homo-tandem device (70 nm front/120 nm back) was fabricated, yielding a high V_{OC} of 1.84 V. Fig. 2i displays the PCE of the tandem device and the estimated STH conversion efficiency relative to the operating voltage. Notably, the V_{MPP} of the solar cell ($\approx$1.54 V) aligns well with the practical voltage required for water electrolysis in 1 M NaOH electrolyte ($\sim$1.5 V). Consequently, this optimized homo-tandem system achieved an estimated STH efficiency of 6.1% without any external bias, demonstrating that precise optical and structural engineering can enable efficient solar fuel production even when using homo-tandem architectures.

3.1.2 System integration and catalytic optimization. To address the high voltage requirements of water electrolysis, Esiner *et al.* developed an "organic artificial leaf" based on a solution-processed triple-junction organic solar cell.[59] Fig. 3a illustrates the device architecture and energy level diagram, comprising a wide bandgap PCDTBT:$PC_{71}BM$ top cell and two identical narrow bandgap PMDPP3T:$PC_{61}BM$ bottom cells connected *via* ZnO/pH-neutral PEDOT interconnecting layers. This series-connected configuration was designed to generate an open-circuit voltage exceeding 2.0 V, providing sufficient potential to drive the water splitting reaction without external bias. The performance of this triple-junction cell when coupled with RuO_2 electrocatalysts was critically dependent on the geometric surface area ratio between the catalyst and the solar cell. Above Fig. 3b present the *J–V* characteristics and transient operation of a small-area device (0.0676 cm^2) connected to large-area catalysts ($\sim$1.2 cm^2), resulting in a high catalyst-to-PV area ratio of approximately 15. Under these conditions, the low local current density on the catalyst surface minimized the kinetic overpotential (0.26 V total), allowing the system to stabilize at an operating voltage (V_{OP}) of 1.49 V. Notably, this operating point closely matched the voltage at the maximum power point ($V_{MPP} = 1.44$ V) of the solar cell, enabling the device to deliver a high photocurrent density of 4.40 mA cm^{-2} and achieve a STH conversion efficiency of 5.4%. However, scaling up the device revealed the critical impact of kinetic constraints. Below Fig. 3b show the performance of a larger-area solar cell (1.7 cm^2) coupled with catalysts of similar size ($\sim$1.2 cm^2), effectively reducing the area ratio to $\sim$0.7. Consequently, the current density on the catalyst surface increased significantly, raising the required overpotential by approximately 0.18 V. This shift forced the system to operate at a higher voltage of 1.67 V, which is far beyond the V_{MPP} (1.40 V) of the solar cell, pushing the device into a region of lower photocurrent extraction. As a result, the operating current density dropped to 2.94 mA cm^{-2}, and the STH efficiency decreased to 3.6%, demonstrating that matching the geometric areas of the PV and catalyst components is as crucial as material selection for efficient solar-to-fuel conversion.

To push the boundaries of OPV-driven water splitting, Kim *et al.* developed a high-efficiency hetero-tandem organic PV–EC system by combining a wide bandgap PM6:IT-M front cell and a narrow bandgap PM6:Y6 back cell.[63] Fig. 3c illustrates the integrated device architecture, where this hetero-tandem OPV, capable of delivering a high V_{OC} of 1.84 V, is coupled with an alkaline electrolyzer consisting of earth-abundant catalysts (Pt or NiMo for HER and $NiFeO_x(OH)_y$ for OER). This configuration was strategically designed to overcome the voltage deficit of single-junction cells while maximizing the spectral utilization of solar energy through complementary absorption. A critical innovation in this work lies in the optimization of the operating point through geometric area engineering. Fig. 3d displays the linear sweep voltammetry (LSV) curves of the OPV and the electrolyzer (EC_1). By adjusting the operating area ratio of the electrolyzer to the PV to approximately 3.6, the authors successfully aligned the operating voltage of the coupled system ($V_{OP} \approx 1.46$ V) with the maximum power point voltage (V_{MPP}) of the tandem solar cell. This precise impedance matching minimized power transfer losses, allowing the system to operate at a high current density of 8.2 mA cm^{-2}, which directly translates to a benchmark STH conversion efficiency of 10%. The robust performance of this optimized system is further highlighted in Fig. 3e, which presents the LSV scan of the integrated OPV–EC device. Even without any external bias (at 0 V), the system maintained a high operating current density of 8.0 mA cm^{-2}, corresponding to an STH efficiency of 9.8%. This result underscores that synergistically combining a high-voltage hetero-tandem absorber with rational system engineerin—specifically, matching the PV and catalyst areas—is a viable pathway to realize highly efficient, unassisted solar hydrogen production using organic photovoltaics.

To address the kinetic challenges of water electrolysis at neutral pH, Elias *et al.* focused on optimizing the FF of the photovoltaic component to maximize power transfer.[61] As aforementioned in Section 2.4, the FF losses in PV are critical to determine the STH efficiency in PV–EC, but the organic PVs and their tandems in particular have low FF, because of bimolecular recombination as a result of low carrier mobility in organic semiconductors.[54] They developed a triple-junction organic solar cell using identical subcells based on the PTB7:$PC_{71}BM$ blend. Fig. 3f presents the *J–V* characteristics of this optimized device. The solar cell achieved a high V_{OC} of 2.13 V and a remarkable FF of 76%. They argued that the simplified fabrication and the homogeneous electrical performance throughout the device can result in high FF by using the homo-tandem of the same three sub-cells. As indicated in the figure, the operating potential required by the catalysts ($\approx$1.7 V) intersects the *J–V* curve very close to the voltage at the maximum power point of the PV, thereby minimizing electrical losses that typically occur when the operating point deviates from the optimal power output. This high-performance photovoltaic device was integrated with a catalyst system designed for neutral pH operation, comprising a glassy carbon-supported RuO_2 anode (GC-RuO_2) and a stainless steel-supported NiMoZn cathode. Fig. 3g illustrates the operational stability of this integrated PV–EC system. The device maintained a stable current density of approximately 4.53 mA cm^{-2} over 1.5 hours, with a V_{OP} stabilizing between 1.70 and 1.75 V. This stable performance confirms that the high voltage and FF of the triple-junction PV cell are sufficient to overcome the thermodynamic

Table 1 Organic tandem PV driven water electrolysis systems

Type	Tandem PV subcells	PV area (cm^2)	Catalyst (HEC‖OEC)	Electrolyte	Stability	Photocurrent (mA cm^{-2})	V_{OP} (V)	STH (%)	Year	Ref.
2T	PF10TBT:PCBM/PDPPTPT:PCBM/PDPPTPT:PCBM	0.09 ∼ 0.16	Pt‖Pt	1 M KOH	—	—	1.70	3.1	2013	58
2T	PCDTBT:$PC_{70}BM$/PMDPP3T:$PC_{60}BM$/PMDPP3T:$PC_{60}BM$	0.0676	RuO_2‖RuO_2	1 M KOH	—	4.4	1.49	5.41	2015	59
2T	PCDTBT:$PC_{70}BM$/PMDPP3T:$PC_{60}BM$/PMDPP3T:$PC_{60}BM$	0.0676	Co_3O_4/NiMoZn	0.1 M KBi	—	3.98	1.56	4.89	2015	59
2T	PCDTBT:$PC_{70}BM$/PMDPP3T:$PC_{60}BM$/PMDPP3T:$PC_{60}BM$	1.7	RuO_2‖RuO_2	1 M KOH	—	2.94	1.67	3.61	2015	59
2T	PTPTIDBT-OD:$PC_{71}BM$/PTPTIDBT-OD:$PC_{71}BM$	0.0676	RuO_2‖RuO_2	1 M KOH	—	3.46	1.50	4.3	2016	60
2T	PTB7:$PC_{71}BM$/PTB7:$PC_{71}BM$/PTB7:$PC_{71}BM$	0.09	SST-NiMoZn‖GC-RuO_2	0.1 M KPi	50 h (79%)[a]	4.53	1.75	6.0	2016	61
2T	PBDTTPD:$PC_{71}BM$/PBDTTPD:$PC_{71}BM$/PBDTTPD:$PC_{71}BM$	0.1	Pt‖Ni foam	1 M NaOH	—	5.4	1.5	6.1	2016	62
2T	PM6:IT-M/PM6:Y6	0.56	Pt‖$NiFeO_x(OH)_y$	1 M KOH	2 h (80.8%)	8.2	1.46	10.0	2022	63
4T	PBQx-TF:FPCC-Br/PBQx-TF:FPCC-Br	1 and 1 (parallel 2illumination)	Pt‖Pt	1M KOH	600 s (72%)	5.62	1.93	6.91	2025	64

[a] Tested under day/night cycles (16 h light/8 h dark) with UV filter.

and kinetic barriers of water splitting in a phosphate buffer solution at pH 7. The efficacy of the system was further validated by quantitative gas analysis. Fig. 3h shows the time-dependent evolution of hydrogen and oxygen gases over a continuous 5-hour operation. The system demonstrated near-unity faradaic efficiency (greater than 98%) for both gases, with a production ratio of H_2 to O_2 close to the theoretical value of 2 : 1. Consequently, this configuration achieved a STH conversion efficiency of approximately 6%, demonstrating that optimizing the fill factor of the light absorber is a decisive strategy for enabling efficient, bias-free water splitting under neutral conditions.

While early-stage efforts established fundamental design strategies such as bandgap engineering and interfacial tuning, recent work has emphasized system-level optimization, including electrode area ratio control and catalyst selection. However, progress remains limited by the inherent performance constraints of organic PV materials. The highest STH efficiency reported for an organic tandem is 10%, achieved with the PM6:IT-M/PM6:Y6 hetero-tandem (Table 1).[63] This figure remains well below the 18% or higher STH values already attained with perovskite-based or III–V-based PV–EC platforms.[66] Consequently, organic tandem PV cells are still regarded as proof-of-concept systems whose STH metrics lag behind those of more mature inorganic counterparts.

3.1.3 Cost-effective wide-bandgap acceptors for solar cells enabling bias-free underwater hydrogen production.

The development of high-performance wide-bandgap acceptors plays a pivotal role in optimizing the front cell of tandem architectures and extending the application scope of PV–EC systems to non-conventional environments. Xiao *et al.* designed and synthesized a novel wide-bandgap acceptor, FPCC-Br, based on a molecular design strategy that minimizes the spatial overlap between the HOMO and LUMO (exchange integral) (Fig. 4a). This approach induced a blue-shift in the absorption spectrum and enhanced V_{OC} (Fig. 4b), yielding a PCE of 13.6% in PBQx-TF:FPCC-Br-based single-junction cells (a record high for bandgaps below 720 nm), 19.3% in ternary cells, and 20.1% in tandem front cells, while effectively mitigating the long-standing trade-off between synthetic cost and device performance.[64]

Owing to its streamlined synthetic route and high yield, FPCC-Br possesses the lowest raw material cost among wide-bandgap acceptors reported to date, and maintains a PCE of 12.2% in large-area (1 cm^2) blade-coating fabrication, underscoring its strong commercialization potential (Fig. 4c and d). Furthermore, this wide-bandgap material is particularly well-suited for applications beyond terrestrial environments, including underwater photovoltaic electrolysis. Xiao *et al.* experimentally demonstrated this by connecting PBQx-TF:FPCC-Br-based organic solar cells in series with Pt electrodes to achieve bias-free underwater hydrogen production. At a water depth of 5 cm, the system delivered a current density of 5.62 mA cm^{-2} at an operating voltage of 1.93 V, achieving a STH efficiency of 6.91% (Fig. 4e).

Despite being fabricated *via* a solution-processed approach, the FPCC-Br-based system exhibited excellent operational and environmental stability. Under thermal stress at 80 °C, it retained approximately 90% of its initial PCE after 1000 hours (Fig. 4f). Even under continuous operation in water, the device maintained 81.5% of its initial efficiency after 1000 hours, demonstrating the remarkable water resistance and long-term stability of the organic semiconductor (Fig. 4g). Furthermore, during electrolysis at a depth of 5 cm, the system sustained 72% of its initial current density for 600 s, while the decay rate of the current density gradually stabilized over time (Fig. 4h). These results highlight that the FPCC-Br-based wide-bandgap acceptor represents a promising candidate for realizing highly reliable PV–EC systems.

3.2 Perovskite tandem PV driven water electrolysis systems

To address the limitations of organic tandem PVs, halide perovskite tandem PVs have emerged as a promising alternative. Perovskite materials offer superior optoelectronic properties—such as high absorption coefficients, long carrier diffusion lengths, and tunable bandgaps—that make them particularly advantageous for tandem solar cell integration.[71,72] In particular, the ability to engineer both wide- and narrow-bandgap perovskite absorbers has enabled the development of monolithic and four-terminal devices capable of delivering high photovoltages and stable operation.[73–81] Combining these strengths, perovskite tandems features have led to significant improvements in STH efficiency, with recent reports exceeding 17%.[39,82] Consequently, all-halide perovskite tandem

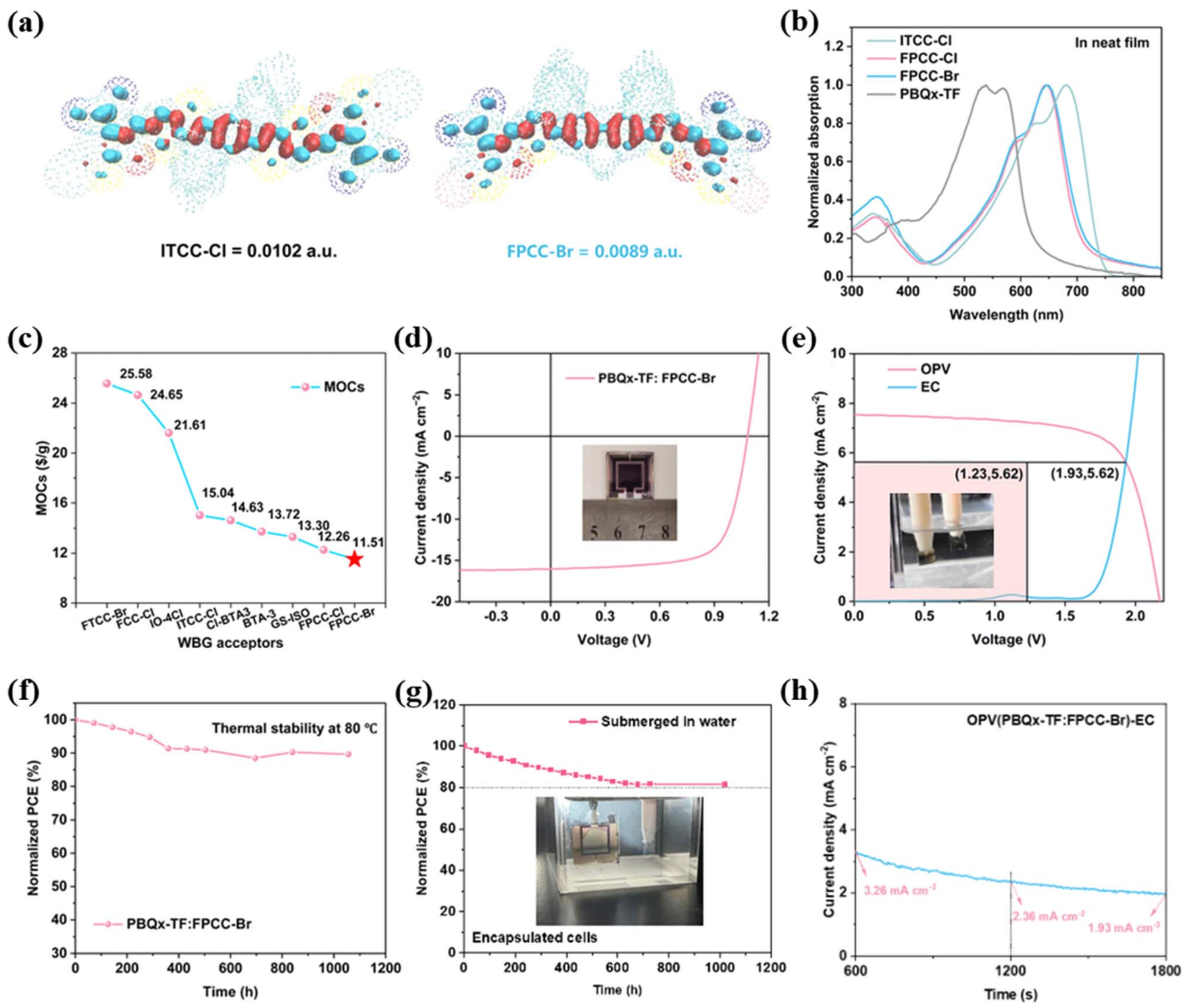

Fig. 4 (a) Overlap and the exchange integrals of HOMO (red) and LUMO (sky blue) distributions. (b) UV-vis absorption spectra of neat films. (c) Material-only cost (MOC) values of typical wide band gap acceptors. (d) J–V curves of a 1 cm^2 device using blade-coating. (e) J–V curves of two OPV cells connected in series and the physical diagram of two series connected cells directly used for underwater photovoltaic electrolysis. (f) Thermal stability of FPCC-Br-based devices at 80 °C. (g) The underwater photovoltaic stability with an FPCC-Br-based cells. (h) The chronoamperometric measurement of two FPCC-Br-based cells connected in series. Adopted with permission.[64] Copyright 2025, The Royal Society of Chemistry.

architectures theoretically allow for optimal efficiency due to the tunability of the band gaps in both subcells and the specialized function of each absorber.[83]

3.2.1 Performance optimization and stability challenges. To address the economic barriers of solar hydrogen production, Luo *et al.* proposed a high-efficiency water splitting device that eliminates expensive noble metal catalysts.[68] Fig. 5a depicts the schematic of this integrated system, where two $\mathrm{CH_3NH_3PbI_3}$ perovskite solar cells are connected in series to form a tandem configuration. This photovoltaic source is wired to Earth-abundant nickel-iron layered double hydroxide (NiFe-LDH) electrodes, which serve as bifunctional catalysts for both the hydrogen and oxygen evolution reactions. The tandem architecture allows the device to generate a high open-circuit voltage of 2.00 V, providing the necessary thermodynamic potential and overpotential to drive water electrolysis without external bias. The efficiency of this system is defined by the coupling between the photovoltaic power output and the electrochemical load. Fig. 5b displays the *J*–*V* characteristics of the perovskite tandem cell alongside the polarization curve of the NiFe-LDH electrolyzer. The intersection of these two curves represents the operating point of the integrated device. Notably, this operating point occurs at a current density of approximately 10 mA $\mathrm{cm^{-2}}$ and a voltage of 1.63 V, which is remarkably close to the maximum power point of the solar cell. This optimal impedance matching minimizes electrical losses and results in a STH conversion efficiency of 12.3%. The capability of the device to perform unassisted water splitting is further confirmed by the photocurrent measurements over time. Fig. 5c shows the current density profile of the integrated system under chopped simulated sunlight with no external bias applied. The device rapidly reaches a stable photocurrent of approximately 10 mA $\mathrm{cm^{-2}}$ upon illumination, maintaining this performance during the initial testing period. This demonstration confirms that solution-processed perovskite photovoltaics combined with low-cost, Earth-abundant catalysts can achieve STH efficiencies exceeding the 10% benchmark required for practical viability.

Building on the potential of perovskite technologies, Wang *et al.* developed a monolithic all-perovskite tandem solar cell specifically optimized for high-voltage water splitting applications.[39] Fig. 5d illustrates the device architecture, which consists of a wide bandgap ($\mathrm{Cs_{0.2}FA_{0.8}Pb(I_{0.6}Br_{0.4})_{3}}$, 1.77 eV) top cell and a narrow bandgap ($\mathrm{Cs_{0.05}FA_{0.7}MA_{0.25}Pb_{0.5}Sn_{0.5}I_{3}}$, 1.25 eV) bottom cell connected by a recombination layer. A critical challenge in such wide-bandgap perovskites is the voltage loss due to non-radiative recombination at the electron transport layer interface. To mitigate this, the authors applied a propane-1,3-diammonium iodide ($\mathrm{PDAI_2}$) surface treatment. As shown in Fig. 5e, the quasi-Fermi level splitting measurements reveal that

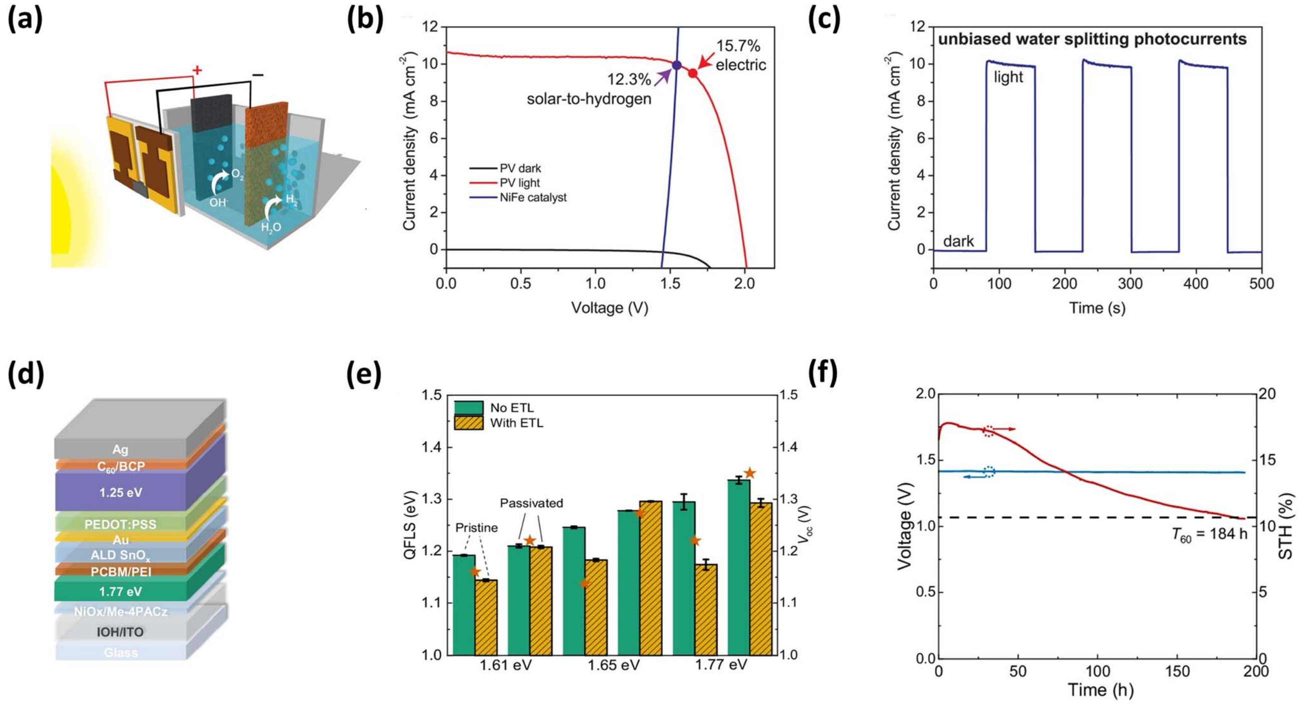

Fig. 5 (a) Schematic diagram of the water-splitting driven by the four-terminal perovskite tandem PV. (b) *J*–*V* curves of the perovskite tandem cell under dark and simulated AM 1.5 G illumination, and the NiFe/Ni foam electrodes in a two-electrode configuration. The illuminated surface area of the perovskite cell was 0.318 cm^2, and the catalyst electrode areas (geometric) were ~5 cm^2 each. (c) Current density–time curve of the integrated water-splitting device without external bias under chopped simulated AM 1.5 G illumination. Adapted with permission.[68] Copyright 2014, American Association for the Advancement of Science. (d) Inverted (p-i-n) perovskite tandem solar cell layout. (e) Quasi-Fermi level splitting of 1.61, 1.65, and 1.77 eV perovskite films. The stars represent the maximum V_{OC} obtained using each perovskite absorber. (f) Voltage (blue) and STH conversion efficiency (red) *vs.* time using the integrated PV–EC system during 192 h continuous operation at approximated 1-sun equivalent light intensity. Adapted with permission.[39] Copyright 2025, Springer Nature.

the $PDAI_2$ treatment significantly reduces energetic losses, enabling the 1.77 eV perovskite to achieve an open-circuit voltage closer to its radiative limit compared to the pristine control. This voltage-optimized tandem cell was integrated into a PV–EC flow cell system to evaluate its performance and stability. Fig. 5f presents the long-term operational data of this system under continuous illumination. The device achieved a record-high STH efficiency of 17.8% at the start of the operation. More importantly, the system demonstrated substantial durability, maintaining stable voltage output and retaining over 60% of its initial efficiency after more than 180 hours of continuous operation. While the voltage remained relatively constant, the gradual decline in STH efficiency was attributed to charge collection losses in the narrow bandgap subcell, highlighting that while interface engineering can maximize initial performance, intrinsic stability of the narrow bandgap perovskite absorber remains a key focus for future improvements.

Stability under heat, moisture, and UV exposure has remained a major challenge for all-perovskite tandem solar cells, prompting extensive efforts to improve both the intrinsic and extrinsic durability of their components. Song *et al.* addressed this by introducing a monolithic all-perovskite tandem configuration that completely eliminates chemically unstable Sn-containing perovskites (Fig. 6a).[67] They utilized a wide bandgap $FA_{0.8}Cs_{0.2}PbBrI_2$ top cell and a narrower bandgap $FA_{0.7}MA_{0.3}PbI_3$ bottom cell, employing fully solution-processed, Pb-only materials. As shown in the theoretical

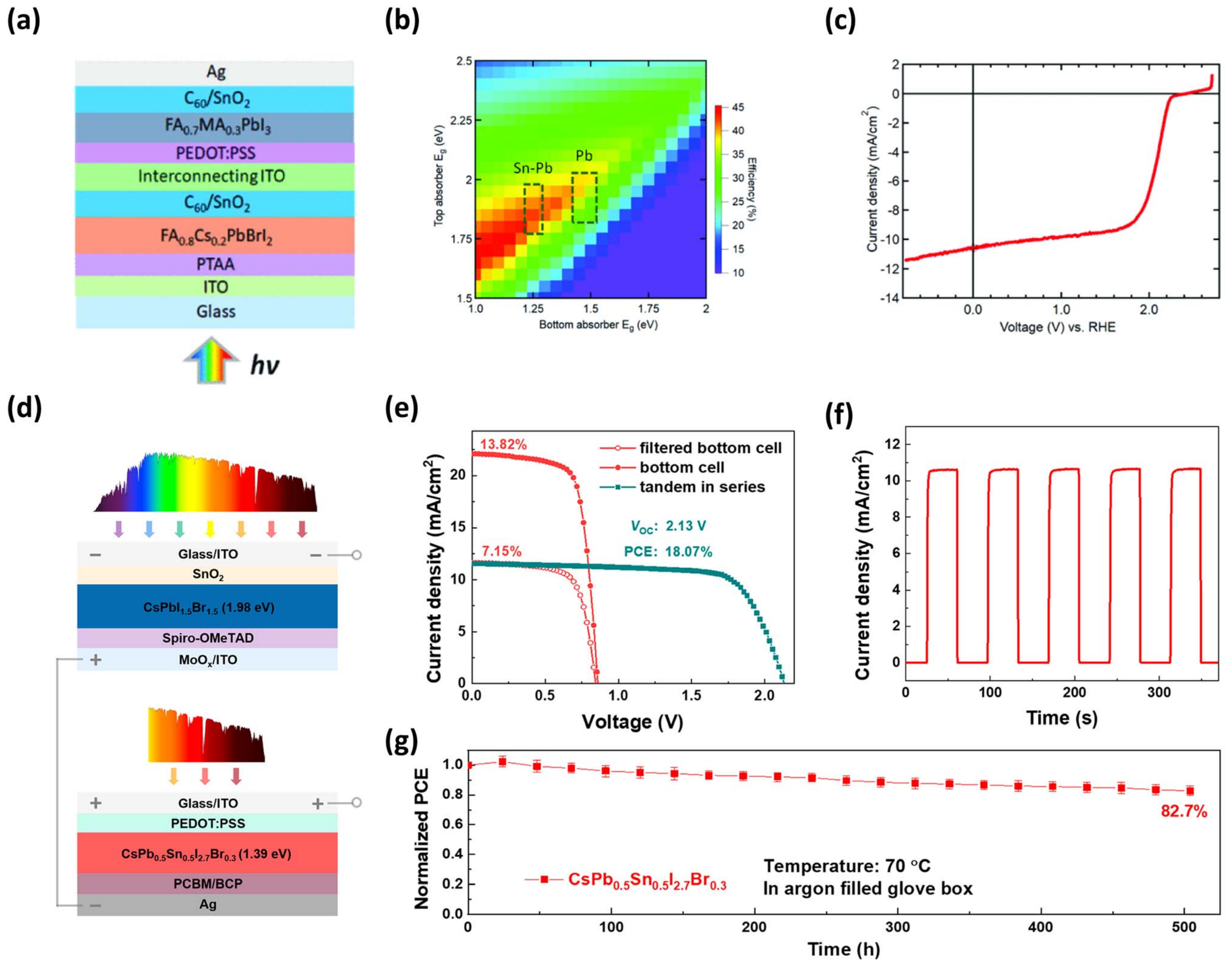

Fig. 6 (a) Schematic illustrations of device structure of a $FA_{0.8}Cs_{0.2}PbBrI_2/FA_{0.7}MA_{0.3}PbI_3$ tandem solar cell. (b) Theoretical efficiency of two-terminal tandem solar cells as a function of top and bottom absorber bandgaps. (c) Linear sweep voltammetry of the perovskite tandem PV driven EC system was performed in a three-electrode setup featuring a Pt cathode and an IrO_x anode.[67] Copyright 2025, IEEE. (d) Schematic diagram of the four-terminal tandem solar cell made by combining a $CsPb_{0.5}Sn_{0.5}I_{2.7}Br_{0.3}$ narrow bandgap perovskite as the bottom subcell and a semi-transparent $CsPbI_{1.5}Br_{1.5}$ wide bandgap perovskite as the top subcell. (e) J–V curves of the integrated four-terminal all-inorganic perovskite tandem solar cell measured using a metallic mask with an aperture area of 0.1 cm^2 under AM 1.5 G illumination with a scan rate of 50 mV s^{-1} in the reverse scan direction. (f) Practical operating current density of the assembled solar water splitting system under chopped AM 1.5 G illumination without external bias. (g) Thermal stability test of un-encapsulated $CsPb_{0.5}Sn_{0.5}I_{2.7}Br_{0.3}$ solar cells measured under 70 °C aging condition in an argon-filled glovebox. Adapted with permission.[43] Copyright 2025, American Chemical Society.

efficiency simulation (Fig. 6b), shifting from the conventional Sn–Pb based bottom cell (left box) to a pure Pb-based one (right box) involves a trade-off in theoretical efficiency limits. The practical viability of this approach for unassisted water splitting was evaluated using a PV–EC system. Fig. 6c presents LSV of the tandem device in a three-electrode configuration. The device exhibits a high onset potential of approximately 2.1 V *vs.* the reversible hydrogen electrode, which provides ample voltage to drive the water splitting reaction. Consequently, the system achieves a photocurrent density of 10.5 mA cm^{-2} at zero bias, confirming that pure Pb-based all-perovskite tandem cells can effectively power unassisted water electrolysis while offering enhanced material stability.

Sun *et al.* demonstrated the first integrated four-terminal tandem solar cell composed entirely of all-inorganic perovskite absorbers to achieve both high efficiency and superior thermal stability.[43] Fig. 6d depicts the schematic of this four-terminal architecture, featuring a semi-transparent inorganic wide-bandgap $CsPbI_{1.5}Br_{1.5}$ top cell and a narrow-bandgap $CsPb_{0.5}Sn_{0.5}I_{2.7}Br_{0.3}$ bottom cell. This all-inorganic design effectively mitigates the volatility issues of organic cations. The photovoltaic performance of this integrated device is shown in Fig. 6e, where the tandem cell achieves a remarkable PCE of 18.07% with a record-high V_{OC} of 2.13 V, making it highly suitable for driving electrochemical loads. Fig. 6f displays the operational stability of this system under chopped illumination, delivering a water-splitting current density of ~10.65 mA cm^{-2} without external bias. This corresponds to a STH efficiency of 13.10%, establishing a new benchmark for all-inorganic perovskite-based solar fuel production. The stability of the inorganic narrow-bandgap absorber, a critical component of this system, is highlighted in Fig. 6g. The unencapsulated device retained over 82% of its initial efficiency after 504 hours of thermal aging at 70 °C, demonstrating exceptional robustness compared to hybrid counterparts.

To harness the high photovoltage potential of perovskite multi-junction cells for practical fuel production, Song *et al.* constructed a PV–EC system driven by a monolithic all-perovskite tandem solar cell.[38] Fig. 7a illustrates the system configuration, where the tandem solar cell is wired to a water electrolyzer comprising a Pt cathode and an IrO_x anode in an acidic electrolyte. This physical separation allows for the optimization of the photovoltaic and electrochemical components independently. The driving force of this system is the high-performance all-perovskite tandem solar cell; as shown in the *J*–*V* characteristics in Fig. 7b, the device delivers a remarkable V_{OC} exceeding 2.1 V and a fill factor over 80%. This high voltage is critical for driving the water splitting reaction without external bias. Consequently, the integrated PV–EC system demonstrates exceptional performance. Fig. 7c presents the operation of the device under chopped 1-sun illumination at zero external bias, where it maintains a steady photocurrent density of approximately 14.1 mA cm^{-2}. This performance translates to a benchmark STH conversion efficiency of 17.2%, confirming that all-perovskite tandem solar cells can effectively power high-efficiency unassisted water splitting.

3.2.2 Perovskite tandem PV driven seawater electrolysis.

Toward practical water electrolysis, it is necessary to check the

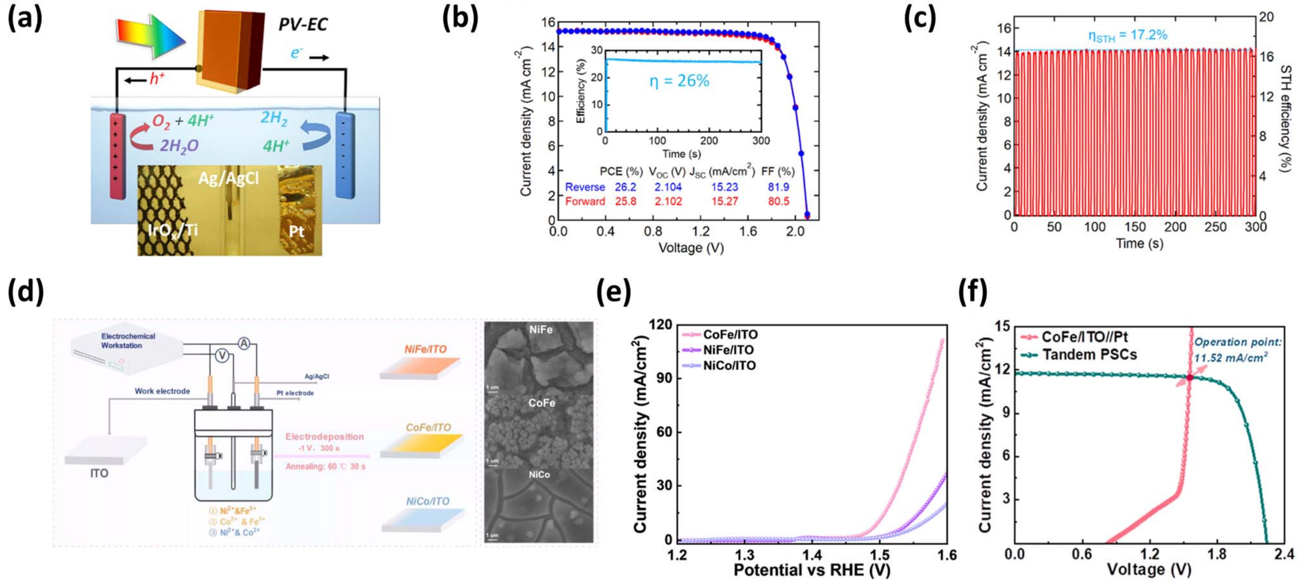

Fig. 7 (a) Schematic diagram of perovskite tandem PV-driven water splitting. The inset is a photo of the IrO_x anode, Pt cathode, and Ag/AgCl reference electrode in an electrolyzer. (b) *J*–*V* curves of an all-perovskite tandem solar cell under simulated 1 sun illumination measured from reverse and forward scans. The inset is the stabilized efficiency measurement of the tandem cell for 300 s. (c) Current density and corresponding STH conversion efficiency of the tandem PV-driven EC device at zero external bias under chopped 1 sun illumination. Adapted with permission.[38] Copyright 2023, American Chemical Society. (d) Schematic diagram of preparation of nonprecious metal catalysts by electrodeposition and corresponding SEM images of NiFe, CoFe, and NiCo on ITO substrates. (e) *J*–*V* characteristics of NiFe, CoFe, and NiCo on ITO substrates, corrected by iR drop. (f) *J*–*V* characteristics of the two-electrode electrochemical cell and the all-perovskite tandem solar cell. Adapted with permission.[69] Copyright 2025, American Chemical Society.

Table 2 Perovskite tandem PV driven water electrolysis systems

Type	Tandem PV subcells	PV area (cm^2)	Catalyst (HEC‖OEC)	Electrolyte	Stability	Photocurrent (mA cm^{-2})	V_{OP} (V)	STH (%)	Year	Ref.
2T	$Cs_{0.2}FA_{0.8}Pb(Br_{0.3}I_{0.7}/FA_{0.7}MA_{0.3}Pb_{0.5}Sn_{0.5}I_3$	0.1	Pt‖IrO$_x$	0.5 M H_2SO_4	120 h (95%)	14.1	—	17	2023	38
2T	$FA_{0.8}Cs_{0.2}PbBrI_2/FA_{0.7}MA_{0.3}PbI_3$	0.12	Pt‖IrO$_x$	0.5 M H_2SO_4	—	~7	—	8.5	2021	67
2T	$Cs_{0.2}FA_{0.8}Pb(I_{0.6}Br_{0.4}/Cs_{0.05}FA_{0.7}MA_{0.25}Pb_{0.5}Sn_{0.5}I_3$	1	Pt/C‖RuO$_2$	H_2O	184 h (over 60%)	14.7	1.42	17.8	2025	39
4T	$CsPbI_{1.5}Br_{1.5}/CsPb_{0.5}Sn_{0.5}I_{2.7}Br_{0.3}$	0.1	Pt/C‖Ni/Fe	1 M KOH	2 h (97.2%)	10.71	1.62	13.1	2022	43
4T	$CH_3NH_3PbI_3/CH_3NH_3PbI_3$	0.318	NiFe-LDH‖NiFe-LDH	1 M NaOH	2 h (~80%)	9.61	1.63	12.3	2014	68
4T	$(FA_{0.7}MA_{0.3})_{0.935}Cs_{0.065}Pb(I_{0.89}Br_{0.11})_3/(FA_{0.7}MA_{0.3})_{0.935}Cs_{0.065}Pb(I_{0.89}Br_{0.11})_3$	1 and 1 (parallel illumination)	Pt‖CoFe	1 M KOH + 0.5 M NaCl	10 h (90%)	11.53	1.56	14.18	2025	69
4T	$(FA_{0.7}MA_{0.3})_{0.935}Cs_{0.065}Pb(I_{0.89}Br_{0.11})_3/(FA_{0.7}MA_{0.3})_{0.935}Cs_{0.065}Pb(I_{0.89}Br_{0.11})_3$	2 and 2 (parallel illumination)	Pt‖NiFe	1 M KOH	—	11.18	—	13.75	2025	70

operation in the seawater environment. While seawater represents 96.5% of water resources from the Earth, its direct utilization in electrolysis is severely hampered by the presence of chloride ions, which trigger the competitive chlorine evolution reaction and accelerate anode corrosion. Addressing these challenges requires electrocatalysts with exceptional selectivity for the OER over chlorine evolution. Li *et al.* proposed a solution by synthesizing a cobalt-iron (CoFe) catalyst on indium tin oxide (ITO) *via* a rapid *in situ* electrodeposition technique (Fig. 7d).[69] This catalyst features a nanoporous architecture that maximizes the active surface area and exhibits superhydrophilicity, facilitating the rapid detachment of gas bubbles during electrolysis. In electrochemical characterization within simulated alkaline seawater, the CoFe electrode demonstrated superior catalytic activity, achieving a low overpotential of 268 mV at 10 mA cm^{-2} (Fig. 7e). This performance notably surpassed that of other bimetallic catalysts such as NiFe (315 mV) and NiCo (330 mV), confirming its high selectivity for OER. To realize unassisted solar hydrogen production, the authors integrated this robust catalyst with perovskite tandem solar cells in a PV–EC configuration. The integrated system operated at a voltage of ~1.56 V with a current density of 11.52 mA cm^{-2}, yielding a remarkable STH efficiency of 14.18% (Fig. 7f). The system demonstrated stable operation for over 10 hours with approximately 90% retention of its initial current density. Furthermore, a comprehensive techno-economic analysis projected a levelized cost of hydrogen of 7.17 \$ kg^{-1}, suggesting a promising pathway toward cost-competitive green hydrogen generation.

All-perovskite tandem structures have rapidly evolved from proof-of-concept devices to highly efficient and stable systems (Table 2). Recent progress includes the development of Sn-free narrow bandgap materials to enhance stability, the adoption of all-inorganic compositions for improved environmental resistance, and detailed investigations of interfacial degradation mechanisms. Nevertheless, the narrow bandgap perovskite subcell often exhibits poor chemical and thermal stability, posing a critical limitation to long-term device reliability.[84] Additionally, the use of similar polar solvents for both subcells often causes solvent-induced damage to the bottom perovskite layer during top-cell deposition, complicating tandem device fabrication.[85]

3.3 Perovskite–organic tandem PV driven water electrolysis systems

Perovskite–organic hybrid tandem structures integrate the complementary strengths of perovskite and organic light absorbers within a single architecture. By combining a wide bandgap perovskite top absorber with a narrow bandgap organic bottom absorber, the hybrid configuration converts high-energy photons efficiently while allowing the organic layer to harvest longer wavelengths that pass through the upper cell. All-organic tandems provide mechanical flexibility and can be fabricated at low temperatures, yet their intrinsically small photovoltage and limited operational stability constrain practical PV–EC use. Conversely, all-perovskite tandems deliver larger voltages and superior charge transport but remain vulnerable to moisture ingress and interfacial degradation, especially in the narrow bandgap perovskites. This spectral splitting not only raises the overall photovoltage to levels sufficient for unbiased water electrolysis but also enhances durability: the inorganic top cell blocks ultraviolet and high-energy radiation, mitigating photochemical stress in the underlying organic layer.[88,89]

3.3.1 Strategies for high-voltage and flexible tandem PVs in water electrolysis applications. Li *et al.* designed a hybrid tandem solar cell combining a wide bandgap perovskite top cell and a narrow bandgap organic bottom cell to secure the high V_{OC} essential for efficient water electrolysis driving.[86] To minimize voltage loss in the 1.74 eV bandgap $Cs_{0.1}(FA_{0.6}MA_{0.4})_{0.9}Pb(I_{0.6}Br_{0.4})_3$ perovskite film, they employed an interfacial passivation strategy using phenmethylammonium bromide (PMABr). As illustrated in the energy level diagram in Fig. 8a, a PMABr layer was inserted between the perovskite and the electron transport layer (PCBM) within the p-i-n configuration (ITO/PTAA/perovskite/PCBM/BCP/Ag). This passivation treatment effectively passivated defects at grain boundaries and surfaces, reducing trap density and suppressing non-radiative recombination, which contributed to achieving an enhanced V_{OC} of 1.22 V in the single-junction device. By monolithically integrating the optimized wide bandgap perovskite top cell with a PBDB-T:SN6IC-4F based organic bottom cell (1.30 eV), a two-terminal perovskite-organic tandem solar cell was fabricated. As evidenced by the *J*–*V* characteristics in Fig. 8b, the rigid substrate-based tandem device achieved a PCE of 15.13%, with a remarkable V_{OC} of 1.85 V, a short-circuit current density (J_{SC}) of 11.52 mA cm^{-2}, and a FF of 70.98%. Notably, the high V_{OC} of 1.85 V sufficiently exceeds the thermodynamic potential required for water splitting (1.23 V), demonstrating the potential to drive an electrolysis system without external bias. To evaluate device stability, the stabilized power output was measured at the maximum power point (1.54 V) as shown in Fig. 8c. The device maintained a stable efficiency of approximately 14.98% for 600 seconds without initial degradation, suggesting that PMABr passivation effectively suppressed light-induced phase segregation common in mixed-halide perovskites, thereby enhancing operational stability. Leveraging the low-temperature processing advantages of the materials, the study also successfully implemented the tandem architecture on a flexible substrate (PET/ITO). As presented in Fig. 8d, the flexible tandem solar cell exhibited excellent performance comparable to its rigid counterpart, recording a PCE of 13.61% and a V_{OC} of 1.80 V. Furthermore, when this flexible tandem device was coupled with a water splitting electrolyzer composed of a NiFe/CNT oxygen evolution catalyst and a Pt/C hydrogen evolution catalyst, it achieved a STH efficiency of 11.21%, as indicated by the operating point in Fig. 8d. These results demonstrate that solution-processed perovskite-organic hybrid tandem

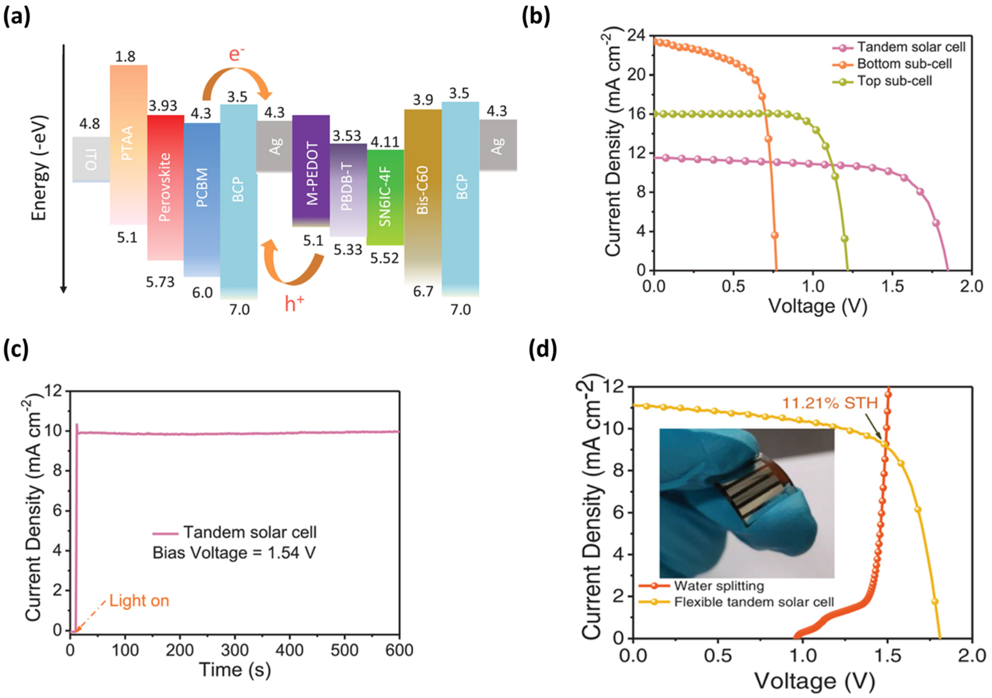

Fig. 8 (a) Energy level diagram of a perovskite–organic tandem solar cell. (b) The *J*–*V* curves of a wide bandgap perovskite $Cs_{0.1}(FA_{0.6}MA_{0.4})_{0.9}Pb(I_{0.6}Br_{0.4})_3$ top subcell, a narrow bandgap PBDB-T:SN61C-4F organic bottom subcell, and the perovskite–organic tandem solar cell under AM 1.5 G illumination. (c) The stabilized photocurrent of the perovskite–organic tandem solar cell was plotted as a function of continuous illumination time at the MPP condition with a steady bias voltage of 1.54 V. (d) The *J*–*V* curves of a flexible perovskite–organic tandem solar cell under simulated AM 1.5 G illumination and NiFe LDH electrodes in a two-electrode system used for water splitting (inset is the photograph of the flexible tandem solar cell). Adapted with permission.[86] Copyright 2020, WILEY-VCH Verlag GmbH & Co. KGaA, Weinheim.

technology is a promising route not only for high-efficiency, but also for light-weight hydrogen production systems such as floating solar fuel production on water as discussed in Section 2.4.

3.3.2 Scalability strategies in monolithic perovskite–organic tandem structure. Zhang *et al.* developed a monolithic perovskite–organic tandem solar cell structure that integrates a methylammonium lead perovskite front cell with a PM6:Y6 organic back cell to achieve high performance through solution processing.[82] As illustrated in the device architecture (Fig. 9a), the two subcells are electrically connected *via* a robust, solvent-resistant interconnecting layer consisting of C_{60}-ionene/Ag/MoO_3, which is designed to form ohmic contacts with low contact resistance. This configuration enables the use of an ultrathin perovskite layer (~100 nm), minimizing lead content while maintaining high efficiency. The photovoltaic performance of the tandem device significantly surpasses that of the individual subcells, as evidenced by the *J*–*V* curves shown in Fig. 9b. The champion tandem device achieved a PCE of 19.2%, with a V_{OC} of 1.92 V, a J_{SC} of 12.6 mA cm^{-2}, and a FF of 79%. The high V_{OC}, which nearly equals the sum of the subcell voltages, confirms the effectiveness of the C_{60}-ionene-based interconnecting layer in facilitating charge recombination. Beyond efficiency, the tandem design offers superior stability against moisture compared to single-junction perovskite cells. When exposed to water droplets, the hydrophobic organic rear cell acts as a protective barrier, preventing the rapid decomposition observed in bare perovskite films. As quantified in Fig. 9c, the

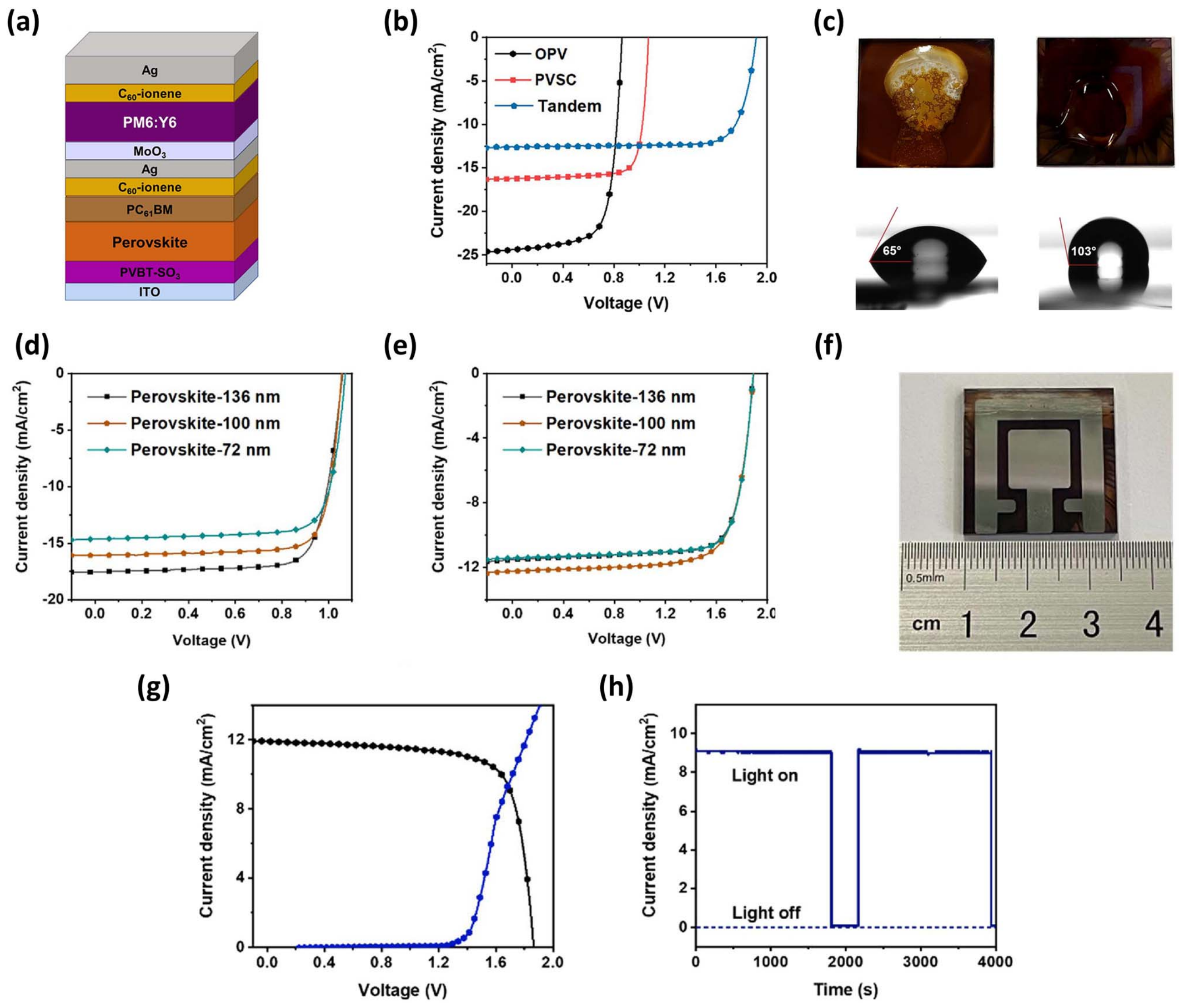

Fig. 9 (a) Device structure of a $MAPbI_{2.95}Cl_{0.05}$/PM6:Y6 tandem solar cell. (b) *J*–*V* curves of $MAPbI_{2.95}Cl_{0.05}$ (denoted as PVSC) and PM6:Y6 (denoted as OPV) subcells, and the tandem solar cell. (c) Photographs of water droplets on the surface of the $MAPbI_{2.95}Cl_{0.05}$ solar cell (left) and the tandem solar cell (right) and corresponding contact angles. (d) *J*–*V* curves of representative $MAPbI_{2.95}Cl_{0.05}$ solar cells and (e) corresponding tandem devices with different perovskite thicknesses. (f) Photograph of a 1 cm^2 tandem solar cell. (g) *J*–*V* curves of the tandem solar cell under simulated AM 1.5 G illumination and the electrochemical cell (Pt||Ni foam) for water splitting. (h) Current density–time curve of the water splitting device under chopped AM 1.5 G illumination. Adapted with permission.[82] Copyright 2022, American Chemical Society.

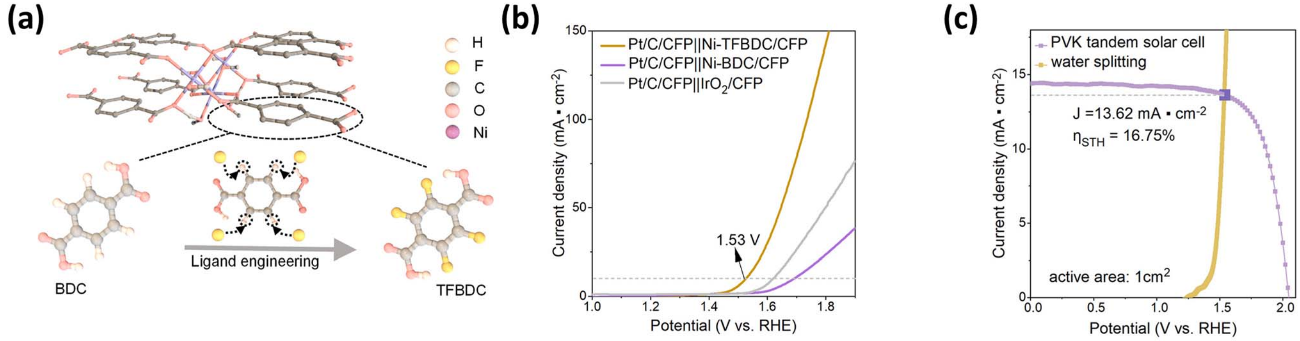

Fig. 10 (a) Illustration of the ligand engineering process used to prepare Ni-TFBDC. (b) Electrochemical water splitting curves of Pt/C/CPF||Ni-BDC/CFP, Pt/C/CPF||IrO$_2$/CFP, and Pt/C/CPF||Ni-TFBDC/CFP cells. (c) *J*–*V* curve of the $FA_{0.8}Cs_{0.2}Pb(I_{0.5}Br_{0.5})_3$/PM6:PM7:Y6:PC$_{71}$BM tandem solar cell and the Pt/C/CPF||Ni-TFBDC/CFP cell. Adapted with permission.[87] Copyright 2023, American Chemical Society.

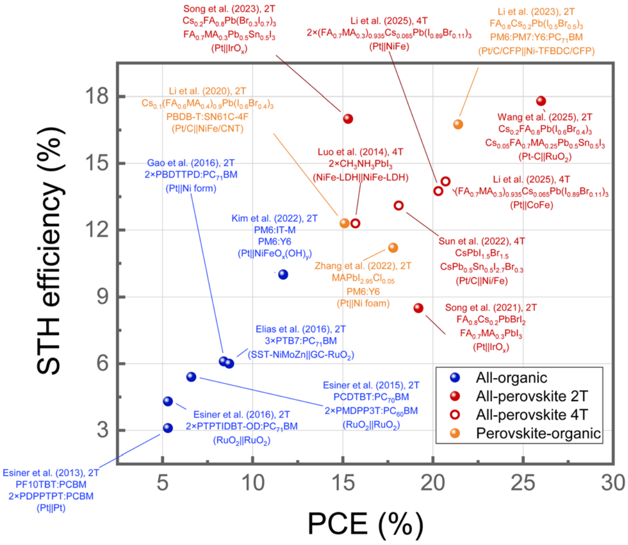

Fig. 11 Summary of the relationship between the PCE of the tandem PVs and STH efficiency of solar water splitting driven by corresponding tandem PVs. The data points differ by the type of tandem PV configurations: all-organic tandem (blue), all-perovskite tandem (red), and perovskite–organic tandem (orange). Annotations indicate the tandem PV subcells, two- or four-terminal (2T or 4T) PV configuration, and catalysts used for the HER and the OER (HEC||OEC).

tandem device exhibited a water contact angle of 103°, significantly higher than the 65° measured for the perovskite single-junction device, attributing the enhanced environmental stability to the hydrophobic nature of the polymer active layer. To optimize the tandem performance, the thickness of the perovskite front cell was carefully tuned to ensure current matching. While reducing the perovskite thickness from approximately 136 nm to 72 nm resulted in a decrease in current for single-junction cells (Fig. 9d), the tandem devices incorporating an ∼100 nm perovskite layer yielded the highest efficiencies (Fig. 9e). This thickness provides an optimal balance, allowing sufficient transparency for the bottom organic cell while maintaining adequate absorption for the top cell, whereas thicker films (∼450 nm) were shown to block a significant portion of the visible light required by the rear cell. Demonstrating the scalability of this approach, the authors successfully fabricated large-area tandem devices (1 cm^2) using the thickness-insensitive interconnecting layer (Fig. 9f), achieving a PCE of 17.8% with high reproducibility. These 1 cm^2 tandem solar cells were further utilized to drive solar-to-hydrogen conversion. The *J*–*V* characteristics in Fig. 9g show the intersection of the tandem cell and the electrolyzer curves, resulting in an operating current density of 9.1 mA cm^{-2} and a STH conversion efficiency of 11.2%. The system demonstrated stable operation under chopped illumination (Fig. 9h), highlighting the potential of these solution-processed perovskite–organic tandem solar cells for efficient and practical green hydrogen production.

3.3.3 Achieving high STH efficiency *via* PV-catalyst optimization. Li *et al.* demonstrated a strategy to enhance the intrinsic activity of metal–organic framework (MOF)

Table 3 Perovskite–organic hybrid tandem PV driven water electrolysis systems

Type	Tandem PV subcells	PV area (cm^2)	Catalyst (HEC||OEC)	Electrolyte	Stability	Photocurrent (mA cm^{-2})	V_{OP} (V)	STH (%)	Year	Ref.
2T	$MAPbI_{2.95}Cl_{0.05}$/PM6:Y6	1	Pt||Ni foam	1 M NaOH	2000 h (91% in N_2)	9.1	1.68	11.2	2022	82
2T	$Cs_{0.1}(FA_{0.6}MA_{0.4})_{0.9}Pb(I_{0.6}Br_{0.4})_3$/PBDB-T:SN61C-4F	0.13	Pt/C||NiFe/CNT	1 M KOH	—	10	1.5	12.3	2020	86
2T	$FA_{0.8}Cs_{0.2}Pb(I_{0.5}Br_{0.5})$/PM6:PM7:Y6:PC$_{71}$BM	1	Pt/C/CFP||Ni-TFBDC/CFP	1 M KOH	—	13.62	—	16.75	2023	87

Table 4 Performance of 2T tandem PV driven water electrolysis systems

	PV						EC							
Year	Tandem PV subcells	PV area (cm^2)	J_{SC} (mA cm^{-2})	V_{OC} (V)	FF (%)	PCE (%)	Catalyst (HEC‖OEC)	Catalyst area (cm^2)	Electrolyte	Stability	Photocurrent (mA cm^{-2})	V_{OP} (V)	STH (%)	Ref.
2013	PF10TBT:PCBM/PDPPTPT:PCBM/PDPPTPT:PCBM	0.09 ∼ 0.16	4.42	2.23	51	5.3	Pt‖Pt	5 cm and 0.35 mm in diameter	1 M KOH	—	—	1.70	3.1	58
2015	PCDTBT:PC$_{70}$BM/PMDPP3T:PC$_{60}$BM/PMDPP3T:PC$_{60}$BM	0.0676	5.81	2.03	57	6.7	RuO$_2$‖RuO$_2$	1.1 and 1.3	1 M KOH	—	4.4	1.49	5.41	59
2015	PCDTBT:PC$_{70}$BM/PMDPP3T:PC$_{60}$BM/PMDPP3T:PC$_{60}$BM	0.0676	5.78	2.00	56	6.5	Co$_3$O$_4$/NiMoZn	1	0.1 M KBi	—	3.98	1.56	4.89	59
2015	PCDTBT:PC$_{70}$BM/PMDPP3T:PC$_{60}$BM/PMDPP3T:PC$_{60}$BM	1.7	5.55	2.03	54	6.1	RuO$_2$‖RuO$_2$	1.2	1 M KOH	—	2.94	1.67	3.61	59
2016	PTPTIDBT-OD:PC$_{71}$BM/PTPTIDBT-OD:PC$_{71}$BM	0.0676	4.14	1.76	73	5.3	RuO$_2$‖RuO$_2$	1.1 and 1.3	1 M KOH	—	3.46	1.50	4.3	60
2016	PTB7:PC$_{71}$BM/PTB7:PC$_{71}$BM/PTB7:PC$_{71}$BM	0.09	5.4	2.13	76	8.7	SST-NiMoZn‖GC-RuO$_2$	—	0.1 M KPi	50 h (79%)[a]	4.53	1.75	6.0	61
2016	PBDTTPD:PC$_{71}$BM/PBDTTPD:PC$_{71}$BM/PBDTTPD:PC$_{71}$BM	0.1	3.95	2.75	68.15	7.42	Pt‖Ni foam	—	1 M NaOH	—	5.4	1.5	6.1	62
2020	Cs$_{0.1}$(FA$_{0.6}$MA$_{0.4}$)$_{0.9}$Pb(I$_{0.6}$Br$_{0.4}$)$_3$/PBDB-T:SN61C-4F	0.13	11.52	1.85	70.98	15.13	Pt/C‖NiFe/CNT	—	1 M KOH	—	10	1.5	12.3	86
2021	FA$_{0.8}$Cs$_{0.2}$PbBrI$_2$/FA$_{0.7}$MA$_{0.3}$PbI$_3$	0.12	11.13	2.153	80	19.2	Pt‖IrO$_x$	—	0.5 M H$_2$SO$_4$	—	∼7	—	8.5	67
2022	PM6:IT-M/PM6:Y6	0.56	9.81	1.84	65	11.7	Pt‖NiFeO$_x$(OH)$_y$	2	1 M KOH	2 h (80.8%)	8.2	1.46	10.0	63
2022	MAPbI$_{2.95}$Cl$_{0.05}$/PM6:Y6	1	12.6	1.92	79	15.6	Pt‖Ni foam	—	1 M NaOH	2000 h (91% in N$_2$)	9.1	1.68	11.2	82
2023	Cs$_{0.2}$FA$_{0.8}$Pb(Br$_{0.3}$I$_{0.7}$/FA$_{0.7}$MA$_{0.3}$Pb$_{0.5}$Sn$_{0.5}$I$_3$	0.1	15.23	2.104	81.9	26.2	Pt‖IrO$_x$	—	0.5 M H$_2$SO$_4$	120 h (95%)	14.1	—	17	38
2023	FA$_{0.8}$Cs$_{0.2}$Pb(I$_{0.5}$Br$_{0.5}$)/PM6:PM7:Y6:PC$_{71}$BM	1	14.23	2.05	73.9	21.38	Pt/C/CFP‖Ni-TFBDC/CFP	—	1 M KOH	—	13.62	—	16.75	87
2025	Cs$_{0.2}$FA$_{0.8}$Pb(I$_{0.6}$Br$_{0.4}$/Cs$_{0.05}$FA$_{0.7}$MA$_{0.25}$Pb$_{0.5}$Sn$_{0.5}$I$_3$	1	16.0	2.08	78	26.0	Pt/C‖RuO$_2$	1	H$_2$O	184 h (over 60%)	14.7	1.42	17.8	39

[a] Tested under day/night cycles (16 h light/8 h dark) with UV filter.

Table 5 Performance of 4T tandem PV driven water electrolysis systems

	PV						EC							
Year	Tandem PV subcells	PV area (cm^2)	J_{SC} (mA cm^{-2})	V_{OC} (V)	FF (%)	PCE (%)	Catalyst (HEC‖OEC)	Catalyst area (cm^2)	Electrolyte	Stability	Photocurrent (mA cm^{-2})	V_{OP} (V)	STH (%)	Ref.
2014	$CH_3NH_3PbI_3/CH_3NH_3PbI_3$	0.318	10.0	2.00	—	15.7	NiFe-LDH‖NiFe-LDH	5	1 M NaOH	2 h (∼80%)	9.61	1.63	12.3	68
2022	$CsPbI_{1.5}Br_{1.5}/CsPb_{0.5}Sn_{0.5}I_{2.7}Br_{0.3}$	0.1	11.56	2.13	73.4	18.07	Pt/C‖Ni/Fe	—	1 M KOH	2 h (97.2%)	10.71	1.62	13.1	43
2025	PBQx-TF:FPCC-Br/PBQx-TF:FPCC-Br	1 and 1 (parallel illumination)	7.90	2.16	69.7	11.9	Pt‖Pt	—	1 M KOH	600 s (72%)	5.62	1.93	6.91	64
2025	$(FA_{0.7}MA_{0.3})_{0.935}Cs_{0.065}Pb(I_{0.89}Br_{0.11})_3/(FA_{0.7}MA_{0.3})_{0.935}Cs_{0.065}Pb(I_{0.89}Br_{0.11})_3$	1 and 1 (parallel illumination)	11.79	2.25	78	20.65	Pt‖CoFe	1	1 M KOH + 0.5 M NaCl	10 h (90%)	11.53	1.56	14.18	69
2025	$(FA_{0.7}MA_{0.3})_{0.935}Cs_{0.065}Pb(I_{0.89}Br_{0.11})_3/(FA_{0.7}MA_{0.3})_{0.935}Cs_{0.065}Pb(I_{0.89}Br_{0.11})_3$	1 and 1 (parallel illumination)	11.62	2.28	—	—	Pt‖NiFe	2	1 M KOH	—	11.18	—	13.75	70

electrocatalysts for oxygen evolution reaction through ligand engineering, which was subsequently integrated with perovskite photovoltaics for efficient solar-to-hydrogen conversion.[87] As illustrated in Fig. 10a, the authors synthesized a fluorinated MOF, denoted as Ni-TFBDC, by substituting the terephthalic acid (BDC) ligands in the nickel-coordinated framework with tetrafluoroterephthalic acid (TFBDC). The substitution of BDC with TFBDC significantly boosts oxygen evolution reaction performance by synergistically modulating the electronic structure, conductivity, and surface properties of the MOF. The introduction of highly electronegative fluorine atoms lowers the oxidation state of nickel centers, as confirmed by X-ray absorption spectroscopy and DFT calculations, which facilitates the reconstruction into highly active γ-NiOOH species during catalysis. This ligand engineering also narrows the bandgap from 0.431 eV to 0.235 eV and drastically reduces charge transfer resistance, thereby accelerating electron transport. Furthermore, steric repulsion between fluorine atoms expands the lattice and reduces crystallinity, leading to a substantial increase in specific surface area and hydrophilicity, while simultaneously shifting the reaction pathway toward the kinetically favorable lattice oxygen mechanism. The electrocatalytic performance of the resulting material was evaluated in a two-electrode water splitting configuration using a Pt/C cathode, as shown in Fig. 10b. The Ni-TFBDC-based cell exhibited superior performance, requiring a voltage of only 1.53 V to drive a current density of 10 mA cm^{-2}, which notably outperformed the control device based on Ni-BDC (1.69 V) and the commercial IrO_2-based system (1.61 V). To achieve unbiased solar water splitting, the Ni-TFBDC electrolyzer was coupled with a high-voltage perovskite–organic tandem solar cell. Fig. 10c displays the intersection of the photovoltaic *J*–*V* curve and the electrolyzer polarization curve, indicating an operating current density of 13.62 mA cm^{-2}. This configuration resulted in a remarkable STH efficiency of 16.75% under AM 1.5 G illumination (Table 3).

4 Conclusion and prospects

In this review, we have examined three types of tandem solar cell architectures that are compatible with solution-based fabrication processes: organic tandem, halide perovskite tandem, and hybrid tandem structures. For each configuration, we investigated how they have been implemented in PV–EC water electrolysis systems, highlighting the specific design strategies and material optimizations employed to enhance device performance and achieve sufficient photovoltage for overall water splitting. Through this analysis, we aimed to elucidate the potential and limitations of each tandem structure in the context of bias-free, efficient solar hydrogen production.

Organic tandem PV structures offer advantages in terms of solution processability and mechanical flexibility. However, due to their intrinsically low charge carrier mobility and limited photovoltage, they face challenges in supplying sufficient voltage for water electrolysis.[90,91] In addition, poor ultraviolet stability and degradation under operational conditions hinder their long-term durability. The maximum STH efficiency stands at 10% driven by the organic–organic tandem PV, representing a relatively modest performance.[63]

Leveraging the superior optoelectronic properties of perovskites, perovskite–perovskite tandem PV configurations have emerged as the most promising candidates for water electrolysis, achieving STH efficiencies approaching 17.8%. However, challenges regarding the difficulty of large-area fabrication remain significant hurdles. Also, the chemical and thermal instability of narrow bandgap perovskites—particularly their sensitivity to moisture and oxygen—negatively impacts device stability and longevity.[92,93]

The perovskite–organic tandem PV structure combines a wide bandgap perovskite top cell with a narrow bandgap organic bottom cell, enabling high operating voltage and broad spectral absorption. Perovskites provide strong visible absorption, while organics enhance near-infrared response. Their compatibility with solution processing and flexible substrates makes this architecture attractive for lightweight, large-area, and bias-free water electrolysis applications. This configuration has already demonstrated sufficient photovoltage for overall water splitting.[94–101] Perovskite–organic tandem PVs achieved a maximum STH efficiency of 16.38%.[87] However, stability remains a challenge due to halide segregation in wide-bandgap perovskites, photodegradation of narrow bandgap polymers, and general vulnerability of the absorber layers to moisture, oxygen, and thermal stress.[102–108] Recent approaches to mitigate these issues include the use of fully inorganic perovskites.[95,100,109–112]

To provide a comprehensive overview of the recent progress, Fig. 11 summarizes the relationship between the PCEs of tandem PVs discussed in this review and the STH efficiencies obtained from water electrolysis systems driven by corresponding tandem PV devices, to enable a more in-depth comparison between PV and EC studies, we include additional extended parameters and present them in chronological order in the newly introduced Tables 4 and 5. The plot reveals a distinct technological evolution: early research was dominated by all-organic tandems with modest efficiencies, whereas recent advancements have been driven by all-perovskite tandems and perovskite–organic tandems, which now occupy the high-efficiency regime. This trend illustrates a clear positive correlation between PV performance and hydrogen production, confirming that high-performance photovoltaic absorbers are a prerequisite for achieving STH values exceeding 15%. Furthermore, as annotated in Fig. 11, these record-breaking efficiencies are being realized using a diverse range of electrocatalysts—from noble metals (*e.g.*, Pt, IrO_x) to earth-abundant transition metal compounds (*e.g.*, NiFe-LDH)—marking a significant step toward practical and cost-effective solar fuel production.

To transition from laboratory-scale proof-of-concept devices to practical, scalable hydrogen production systems, future research must converge on the following critical areas:

4.1 Intrinsic stability of solution processable PV materials

The stability demands placed on solution-processable PV materials in integrated PV–EC systems are fundamentally distinct from those encountered in grid-connected operation. For perovskite light absorbers, the central concern is the diurnal cycling through multiple voltage states inherent to direct-coupled operation: at dawn and dusk, when the electrolyser has not yet reached its onset threshold, the perovskite cell dwells near V_{OC}, precisely the condition shown to maximise charge accumulation, accelerate ion migration, and produce the lowest operational stability, meaning the device experiences its most damaging electrical state exactly when it is performing no useful water electrolysis. For organic light absorbers, the critical threats are thermally driven morphological coarsening of the BHJ under outdoor temperature cycling, which simultaneously degrades FF and J_{SC}, and the well-documented burn-in efficiency loss in the first tens to hundreds of hours of operation. They carry a uniquely severe consequence in PV–EC: if efficiency loss is sufficient to shift the operating voltage below the electrolyser onset threshold, hydrogen production ceases entirely rather than merely declining. Compounding both material classes is the proximity of the liquid electrolyte environment, which imposes moisture ingress and chemical compatibility requirements on encapsulation that far exceed those of standard photovoltaic deployment, alongside the toxicity constraint of preventing lead or organic component leaching into the electrolyte. Critically, no current stability standard captures these coupled stressors, as none incorporates variable-voltage operation along an electrolyser load line, start-stop cycling with open-circuit dwell, or interfacial chemical exposure; prospective work must therefore develop PV–EC specific accelerated stress test protocols that treat the photovoltaic and electrochemical subsystems as a coupled degrading system rather than independently qualified components.

4.2 System-level integration and geometric optimization

Achieving high-performance integrated PV–EC systems based on solution-processable perovskite and organic absorbers demands a co-design philosophy in which geometric, catalytic, and system-level parameters are treated as primary optimisation variables from the outset, rather than as secondary engineering adjustments applied to independently optimised components. The most critical geometric variable is the PV-to-electrolyser area ratio, which determines the current density at which the electrolyser operates. For tandem architectures combining perovskite front cells with organic rear cells, photocurrent matching between subcells introduces an additional geometric constraint: optical and parasitic losses at the interconnection layer directly limit the current delivered to the electrolyser, and sub-optimal matching carries a threshold consequence in PV–EC operation whereby the system ceases hydrogen production entirely rather than operating at reduced efficiency. Crucially, the cost reduction potential uniquely offered by solution-processable PV materials can only be fully realised at the system level if the electrocatalyst cost is addressed in parallel, the replacement of precious metal catalysts such as platinum and iridium oxide with earth-abundant alternatives, including transition metal phosphides, sulfides, and layered double hydroxides for the hydrogen and oxygen evolution reactions respectively, is therefore not merely a materials science objective but a system-level economic necessity, since retaining rare-metal catalysts in a system built around low-cost solution-processed absorbers creates a cost asymmetry that undermines the economic case for the entire integration strategy. Prospectively, realising the full optimisation potential of these materials will require integrated multiphysics modelling frameworks that simultaneously treat optical design, electrochemical load matching, area ratio, earth-abundant catalyst selection, encapsulation geometry, and deployment configuration as a coupled optimisation problem: a level of co-design sophistication that the field has not yet systematically achieved.

4.3 Scalability and technical challenges

Solution-processed 2T tandem PV devices have recently emerged as a promising platform for highly efficient solar-driven hydrogen production, demonstrating sufficiently high photovoltage and excellent fill factor for unbiased water splitting at the laboratory cell level. Representative devices have reported V_{OC} exceeding 1.8 V, in some cases surpassing 2 V, together with FF over 80%, clearly indicating the potential for self-sustained water electrolysis without external bias. However, extending such performance to large-area modules requires precise control of film formation uniformity, which is an inherent limitation of solution-based processes. It also demands careful optimization of the resistance–transmittance characteristics of transparent electrodes, interfacial quality, and current matching between serially connected subcells. During scaling, factors such as increased sheet resistance of transparent electrodes, coating non-uniformity, crystallization variability, and interfacial defects tend to accumulate, resulting in higher series resistance and non-ideal recombination losses that degrade FF and sometimes V_{OC}.[38] Moreover, in the 2T tandem structure, current mismatch between subcells constrains overall operating current, so even minor deviations in optical or electrical matching can directly lead to significant module performance losses. While such losses primarily appear as reduced power output in standalone PV systems, they become far more detrimental in directly coupled PV–EC systems, where the operating voltage must remain above the practical water electrolysis threshold to maintain unassisted operation and steady hydrogen generation.[113] Therefore, maintaining the high photovoltage and fill factor achieved at small scales in module-level devices should be regarded not merely as a goal for efficiency enhancement but as a prerequisite for stable, system-level hydrogen production.[114] In particular, for PV–EC systems based on solution-processed tandem devices, performance losses caused by film non-uniformity, current mismatch, and interfacial defects during large-area fabrication are critical. Consequently, research on large-area implementation remains markedly insufficient. This limitation acts as a key bottleneck, hindering the translation of small-area high performance to module-scale devices and thereby delaying stable hydrogen production at the system level. To achieve this, process stabilization strategies that can precisely control film uniformity and interfacial quality in large-area solution processing are essential. In particular, (i) controlling the fluid dynamics during coating to ensure meniscus stability, (ii) securing interlayer process compatibility through immiscible or carefully designed orthogonal solvent combinations, and (iii) employing flash drying, infrared, or thermal-assisted drying to regulate the crystallization of the top layer while mitigating thermal stress on the underlying layers are required as part of scalable and refined solution-processing techniques.[115,116] Meanwhile, (iv) the development of low-resistance transparent electrodes and highly efficient interconnecting layer/recombination junctions, (v) the use of bandgap combinations and optical–electrical designs less sensitive to spectral variations, and (vi) the optimization of laser scribing-based monolithic interconnections serves as critical factors in minimizing resistive and interconnection losses during large-area module fabrication.[117,118] Module design must further ensure voltage retention and current scalability through serial stack matching and serial expansion. In this architecture, scalability should not rely solely on increasing the PV voltage itself but rather on proportional co-scaling of PV module voltage and electrolyser stack voltage through serial interconnection.[119] Furthermore, achieving long-term durability requires encapsulation and interfacial stabilization techniques that suppress ion migration and interfacial degradation, together with the establishment of accelerated lifetime evaluation protocols under combined thermal, light, and electrical stresses.[120] Beyond efficiency enhancement, process development should also account for manufacturing yield, reproducibility, PV–EC integration, and techno-economic metrics based on the levelized cost of hydrogen.[121] With these technological advances and systematic process control, solution-processed 2T perovskite tandem PV–EC systems are expected to realize both high-voltage operation and efficient unassisted water electrolysis, paving the way for practical large-area manufacturing and sustainable STH production.

In conclusion, while solution-processed tandem PV–EC systems have made remarkable strides in efficiency, the focus must now shift toward holistic system engineering that simultaneously addresses stability, scalability, and cost. By converging material innovations with rational system design, these technologies hold the potential to become a cornerstone of the future green hydrogen economy.

Author contributions

H.-B. K. led the review and carried out the investigation and visualization. W. C. surveyed the relevant literature. T. H. L. contributed to conceptualization and edited the manuscript.

Conflicts of interest

There are no conflicts to declare.

Data availability

No primary research results, software or code have been included and no new data were generated or analysed as part of this review.

Acknowledgements

This work was supported by a 2-Year Research Grant of Pusan National University.

Notes and references

1 A. M. Oliveira, R. R. Beswick and Y. Yan, *Curr. Opin. Chem. Eng.*, 2021, **33**, 100701.
2 A. G. Olabi and M. A. Abdelkareem, *Renew. Sustain. Energy Rev.*, 2022, **158**, 112111.
3 B. C. Tashie-Lewis and S. G. Nnabuife, *Chem. Eng. J. Adv.*, 2021, **8**, 100172.
4 H. H. Cho, V. Strezov and T. J. Evans, *Sustain. Mater. Technol.*, 2023, **35**, e00567.
5 N. Ma, W. Zhao, W. Wang, X. Li and H. Zhou, *Int. J. Hydrogen Energy*, 2024, **50**, 379–396.
6 G. Squadrito, G. Maggio and A. Nicita, *Renewable Energy*, 2023, **216**, 119041.
7 F. Urbain, V. Smirnov, J.-P. Becker, U. Rau, J. Ziegler, B. Kaiser, W. Jaegermann and F. Finger, *Sol. Energy Mater. Sol. Cells*, 2015, **140**, 275–280.
8 S. Hu, C. Xiang, S. Haussener, A. D. Berger and N. S. Lewis, *Energy Environ. Sci.*, 2013, **6**, 2984.
9 K. Zhang, M. Ma, P. Li, D. H. Wang and J. H. Park, *Adv. Energy Mater.*, 2016, **6**, 1600602.
10 J. Jia, L. C. Seitz, J. D. Benck, Y. Huo, Y. Chen, J. W. Ng, T. Bilir, J. S. Harris and T. F. Jaramillo, *Nat. Commun.*, 2016, **7**, 13237.
11 C. Jiang, S. J. A. Moniz, A. Wang, T. Zhang and J. Tang, *Chem. Soc. Rev.*, 2017, **46**, 4645–4660.
12 F. Finger, K. Welter, F. Urbain, V. Smirnov, B. Kaiser and W. Jaegermann, *Z. Phys. Chem.*, 2020, **234**, 1055–1095.
13 A. Vilanova, P. Dias, T. Lopes and A. Mendes, *Chem. Soc. Rev.*, 2024, **53**, 2388–2434.
14 F. Qureshi and M. Tahir, *Int. J. Hydrogen Energy*, 2024, **69**, 760–776.
15 A. F. Palmstrom, G. E. Eperon, T. Leijtens, R. Prasanna, S. N. Habisreutinger, W. Nemeth, E. A. Gaulding, S. P. Dunfield, M. Reese, S. Nanayakkara, T. Moot, J. Werner, J. Liu, B. To, S. T. Christensen, M. D. McGehee, M. F. A. M. van Hest, J. M. Luther, J. J. Berry and D. T. Moore, *Joule*, 2019, **3**, 2193–2204.
16 Y. Jiang and Y. Qi, *Mater. Chem. Front.*, 2021, **5**, 4833–4850.
17 L. Mao, J. Tong, S. Xiong, F. Jiang, F. Qin, W. Meng, B. Luo, Y. Liu, Z. Li, Y. Jiang, C. Fuentes-Hernandez, B. Kippelen and Y. Zhou, *J. Mater. Chem. A*, 2017, **5**, 3186–3192.
18 H. Lai, J. Luo, Y. Zwirner, S. Olthof, A. Wieczorek, F. Ye, Q. Jeangros, X. Yin, F. Akhundova, T. Ma, R. He, R. K. Kothandaraman, X. Chin, E. Gilshtein, A. Müller, C. Wang, J. Thiesbrummel, S. Siol, J. M. Prieto, T. Unold, M. Stolterfoht, C. Chen, A. N. Tiwari, D. Zhao and F. Fu, *Adv. Energy Mater.*, 2022, **12**, 2202438.
19 M. Raïssi, S. Wageh, A. A. Al-Ghamdi and D. Rousseau, *J. Mater. Chem. A*, 2023, **11**, 25578–25594.
20 H. Liu, M. H. Yu, C. C. Lee, X. Yu, Y. Li, Z. Zhu, C. C. Chueh, Z. a. Li and A. K. Y. Jen, *Adv. Mater. Technol.*, 2021, **6**, 2000960.
21 P. Subudhi and D. Punetha, *Prog. Photovolt. Res. Appl.*, 2023, **31**, 753–789.
22 Y. Sun, T. Liu, Y. Kan, K. Gao, B. Tang and Y. Li, *Small Sci.*, 2021, **1**, 2100001.
23 N. Ahn and M. Choi, *Adv. Sci.*, 2024, **11**, e2306110.
24 D. Zhang, D. Li, Y. Hu, A. Mei and H. Han, *Commun. Mater.*, 2022, **3**, 58.
25 Z. Ni, H. Jiao, C. Fei, H. Gu, S. Xu, Z. Yu, G. Yang, Y. Deng, Q. Jiang, Y. Liu, Y. Yan and J. Huang, *Nat. Energy*, 2021, **7**, 65–73.
26 Y. Zhao, Z. Wu, X. Liu, Z. Zhong, R. Zhu and J. Yu, *J. Mater. Chem. C*, 2021, **9**, 13972–13980.
27 A. J. Clarke, J. Luke, R. Meitzner, J. Wu, Y. Wang, H. K. H. Lee, E. M. Speller, H. Bristow, H. Cha, M. J. Newman, K. Hooper, A. Evans, F. Gao, H. Hoppe, I. McCulloch, U. S. Schubert, T. M. Watson, J. R. Durrant, W. C. Tsoi, J.-S. Kim and Z. Li, *Cell Rep. Phys. Sci.*, 2021, **2**, 100498.
28 J. K. Norskov, J. Rossmeisl, A. Logadottir, L. Lindqvist, J. R. Kitchin, T. Bligaard and H. Jonsson, *J. Phys. Chem. B*, 2004, **108**, 17886–17892.
29 J. Rossmeisl, Z. W. Qu, H. Zhu, G. J. Kroes and J. K. Nørskov, *J. Electroanal. Chem.*, 2007, **607**, 83–89.
30 S. Zhou, N. Liu, Z. Wang and J. Zhao, *ACS Appl. Mater. Interfaces*, 2017, **9**, 22578–22587.
31 K. Zeng and D. Zhang, *Prog. Energy Combust. Sci.*, 2010, **36**, 307–326.
32 C. Xiang, K. M. Papadantonakis and N. S. Lewis, *Mater. Horiz.*, 2016, **3**, 169–173.
33 Y. Wang, Y. Wu, J. Schwartz, S. H. Sung, R. Hovden and Z. Mi, *Joule*, 2019, **3**, 2444–2456.
34 T. Baumeler, N. Arora, A. Hinderhofer, S. Akin, A. Greco, M. Abdi-Jalebi, R. Shivanna, R. Uchida, Y. Liu, F. Schreiber, S. M. Zakeeruddin, R. H. Friend, M. Graetzel and M. I. Dar, *J. Phys. Chem. Lett.*, 2020, **11**, 10188–10195.
35 K. T. Fountaine, H. J. Lewerenz and H. A. Atwater, *Nat. Commun.*, 2016, **7**, 13706.
36 J.-F. Guillemoles, T. Kirchartz, D. Cahen and U. Rau, *Nat. Photonics*, 2019, **13**, 501–505.
37 S. Rühle, *Sol. Energy*, 2016, **130**, 139–147.
38 Z. Song, C. Li, L. Chen, K. Dolia, S. Fu, N. Sun, Y. Li, K. Wyatt, J. L. Young, T. G. Deutsch and Y. Yan, *ACS Energy Lett.*, 2023, **8**, 2611–2619.
39 J. Wang, B. Branco, W. H. M. Remmerswaal, S. Hu, N. R. M. Schipper, V. Zardetto, L. Bellini, N. Daub, M. M. Wienk, A. Wakamiya, H. J. Snaith and R. A. J. Janssen, *Nat. Commun.*, 2025, **16**, 174.
40 W. E. McMahon, J. F. Geisz, J. Buencuerpo and E. L. Warren, *Sustain. Energy Fuels*, 2023, **7**, 461–470.
41 R. Fan, S. Cheng, G. Huang, Y. Wang, Y. Zhang, S. Vanka, G. A. Botton, Z. Mi and M. Shen, *J. Mater. Chem. A*, 2019, **7**, 2200–2209.
42 R. Witteck, J. F. Geisz, E. L. Warren and W. E. McMahon, *Sol. RRL*, 2023, **8**, 2300782.
43 Q. Sun, Z. Zhang, T. Zhang, Y. Feng, A. Gu, H. Yu, M. Zhang, X. L. Zhang, J. Zhu, Y. Shen and M. Wang, *ACS Energy Lett.*, 2022, **7**, 4215–4223.

44 Z. Shokrollahi, M. Piralaee and A. Asgari, *Sci. Rep.*, 2024, **14**, 11515.

45 B. Abdollahi Nejand, D. B. Ritzer, H. Hu, F. Schackmar, S. Moghadamzadeh, T. Feeney, R. Singh, F. Laufer, R. Schmager, R. Azmi, M. Kaiser, T. Abzieher, S. Gharibzadeh, E. Ahlswede, U. Lemmer, B. S. Richards and U. W. Paetzold, *Nat. Energy*, 2022, **7**, 620–630.

46 E. Raza and Z. Ahmad, *Energy Rep.*, 2022, **8**, 5820–5851.

47 Gurudayal, D. Sabba, M. H. Kumar, L. H. Wong, J. Barber, M. Gratzel and N. Mathews, *Nano Lett.*, 2015, **15**, 3833–3839.

48 V. A. Martinez Lopez, H. Ziar, J. W. Haverkort, M. Zeman and O. Isabella, *Renew. Sustain. Energy Rev.*, 2023, **182**, 113407.

49 C. Chen, L. Wang, W. Xia, K. Qiu, C. Guo, Z. Gan, J. Zhou, Y. Sun, D. Liu, W. Li and T. Wang, *Nat. Commun.*, 2024, **15**, 6865.

50 M. A. Green, E. D. Dunlop, M. Yoshita, N. Kopidakis, K. Bothe, G. Siefer, X. Hao and J. Y. Jiang, *Prog. Photovolt. Res. Appl.*, 2025, **33**, 795–810.

51 J. Wang, J. Li, Y. Wang, J. Ren, P. Bi, H. Li, J. Dai, S. Zhang and J. Hou, *Adv. Mater.*, 2025, **37**, e10378.

52 Z. Liu, R. Lin, M. Wei, M. Yin, P. Wu, M. Li, L. Li, Y. Wang, G. Chen, V. Carnevali, L. Agosta, V. Slama, N. Lempesis, Z. Wang, M. Wang, Y. Deng, H. Luo, H. Gao, U. Rothlisberger, S. M. Zakeeruddin, X. Luo, Y. Liu, M. Gratzel and H. Tan, *Nat. Mater.*, 2025, **24**, 252–259.

53 X. Jiang, S. Qin, L. Meng, G. He, J. Zhang, Y. Wang, Y. Zhu, T. Zou, Y. Gong, Z. Chen, G. Sun, M. Liu, X. Li, F. Lang and Y. Li, *Nature*, 2024, **635**, 860–866.

54 T. H. Lee, Y. Dong, R. A. Pacalaj, S. Y. Park, W. Xu, J. S. Kim and J. R. Durrant, *Adv. Funct. Mater.*, 2022, **32**, 2208001.

55 M. V. Khenkin, E. A. Katz, A. Abate, G. Bardizza, J. J. Berry, C. Brabec, F. Brunetti, V. Bulović, Q. Burlingame, A. Di Carlo, R. Cheacharoen, Y.-B. Cheng, A. Colsmann, S. Cros, K. Domanski, M. Dusza, C. J. Fell, S. R. Forrest, Y. Galagan, D. Di Girolamo, M. Grätzel, A. Hagfeldt, E. von Hauff, H. Hoppe, J. Kettle, H. Köbler, M. S. Leite, S. Liu, Y.-L. Loo, J. M. Luther, C.-Q. Ma, M. Madsen, M. Manceau, M. Matheron, M. McGehee, R. Meitzner, M. K. Nazeeruddin, A. F. Nogueira, Ç. Odabaşı, A. Osherov, N.-G. Park, M. O. Reese, F. De Rossi, M. Saliba, U. S. Schubert, H. J. Snaith, S. D. Stranks, W. Tress, P. A. Troshin, V. Turkovic, S. Veenstra, I. Visoly-Fisher, A. Walsh, T. Watson, H. Xie, R. Yıldırım, S. M. Zakeeruddin, K. Zhu and M. Lira-Cantu, *Nat. Energy*, 2020, **5**, 35–49.

56 M. Cai, Y. Wu, H. Chen, X. Yang, Y. Qiang and L. Han, *Adv. Sci.*, 2017, **4**, 1600269.

57 V. Andrei, G. M. Ucoski, C. Pornrungroj, C. Uswachoke, Q. Wang, D. S. Achilleos, H. Kasap, K. P. Sokol, R. A. Jagt, H. Lu, T. Lawson, A. Wagner, S. D. Pike, D. S. Wright, R. L. Z. Hoye, J. L. MacManus-Driscoll, H. J. Joyce, R. H. Friend and E. Reisner, *Nature*, 2022, **608**, 518–522.

58 S. Esiner, H. van Eersel, M. M. Wienk and R. A. Janssen, *Adv. Mater.*, 2013, **25**, 2932–2936.

59 S. Esiner, R. E. M. Willems, A. Furlan, W. Li, M. M. Wienk and R. A. J. Janssen, *J. Mater. Chem. A*, 2015, **3**, 23936–23945.

60 S. Esiner, G. W. P. van Pruissen, M. M. Wienk and R. A. J. Janssen, *J. Mater. Chem. A*, 2016, **4**, 5107–5114.

61 X. Elias, Q. Liu, C. Gimbert-Suriñach, R. Matheu, P. Mantilla-Perez, A. Martinez-Otero, X. Sala, J. Martorell and A. Llobet, *ACS Catal.*, 2016, **6**, 3310–3316.

62 Y. Gao, V. M. Le Corre, A. Gaitis, M. Neophytou, M. A. Hamid, K. Takanabe and P. M. Beaujuge, *Adv. Mater.*, 2016, **28**, 3366–3373.

63 Y. K. Kim, T. H. Lee, J. Yeop, W. J. Byun, J. H. Kim, J. Y. Kim and J. S. Lee, *Appl. Catal., B*, 2022, **309**, 121237.

64 Y. Xiao, J. Wang, Y. Cui, Y. Wang, Z. Chen, S. Cheng, H. Yuan, J. Qiao, Y. Yang, W. Wang, N. Yang, Y. Yu, R. Yu, X. Hao and J. Hou, *Energy Environ. Sci.*, 2025, **18**, 3259–3268.

65 Y. Fu, T. H. Lee, Y. C. Chin, R. A. Pacalaj, C. Labanti, S. Y. Park, Y. Dong, H. W. Cho, J. Y. Kim, D. Minami, J. R. Durrant and J. S. Kim, *Nat. Commun.*, 2023, **14**, 1870.

66 Z. Li, S. Fang, H. Sun, R. J. Chung, X. Fang and J. H. He, *Adv. Energy Mater.*, 2023, **13**, 2203019.

67 Z. N. Song, C. W. Li, L. Chen, S. Rijal, J. L. Young, T. G. Deutsch and Y. F. Yan, *IEEE Photovoltaic Spec. Conf.*, 2021, **20–25**, 2222–2225.

68 J. Luo, J. H. Im, M. T. Mayer, M. Schreier, M. K. Nazeeruddin, N. G. Park, S. D. Tilley, H. J. Fan and M. Gratzel, *Science*, 2014, **345**, 1593–1596.

69 Y. Li, Y. Li, Z. Ma, K. Yue, Q. Yang, X. Li, Q. Zhang, F. Gou, H. Du, C. Cheng, M. Mao, D. Xiang, Z. Lv, K. Liu, B. Chen, R. Xu, Q. Yin, B. Luo, J. Zhan, K. Sun, C. Tang and Z. Pan, *ACS Appl. Mater. Interfaces*, 2025, **17**, 32530–32543.

70 Y. Li, Z. Ma, S. Hou, X. Li, S. Wang, Z. Du, Y. Chen, Q. Zhang, Y. Li, Q. Yang, Z. Huang, L. Bai, H. Yu, Q. Liu, Y. Xiang, M. Zhang, J. Yu, J. Xie, Y. Zhou, C. Tang, K. Sun and L. Ding, *J. Colloid Interface Sci.*, 2025, **677**, 599–609.

71 S. D. Stranks, G. E. Eperon, G. Grancini, C. Menelaou, M. J. Alcocer, T. Leijtens, L. M. Herz, A. Petrozza and H. J. Snaith, *Science*, 2013, **342**, 341–344.

72 C. C. Stoumpos, C. D. Malliakas and M. G. Kanatzidis, *Inorg. Chem.*, 2013, **52**, 9019–9038.

73 S. Tan, C. Li, C. Peng, W. Yan, H. Bu, H. Jiang, F. Yue, L. Zhang, H. Gao and Z. Zhou, *Nat. Commun.*, 2024, **15**, 4136.

74 J. Zhou, H. Qiu, T. Wen, Z. He, C. Zou, Y. Shi, L. Zhu, C. C. Chen, G. Liu, S. Yang, F. Liu and Z. Yang, *Adv. Energy Mater.*, 2023, **13**, 2300968.

75 C. Li, L. Chen, F. Jiang, Z. Song, X. Wang, A. Balvanz, E. Ugur, Y. Liu, C. Liu, A. Maxwell, H. Chen, Y. Liu, Z. Wang, P. Xia, Y. Li, S. Fu, N. Sun, C. R. Grice, X. Wu, Z. Fink, Q. Hu, L. Zeng, E. Jung, J. Wang, S. M. Park, D. Luo, C. Chen, J. Shen, Y. Han, C. A. R. Perini, J.-P. Correa-Baena, Z.-H. Lu, T. P. Russell, S. De Wolf, M. G. Kanatzidis, D. S. Ginger, B. Chen, Y. Yan and E. H. Sargent, *Nat. Energy*, 2024, **9**, 1388–1396.

76 T. Leijtens, R. Prasanna, K. A. Bush, G. E. Eperon, J. A. Raiford, A. Gold-Parker, E. J. Wolf, S. A. Swifter,

C. C. Boyd, H.-P. Wang, M. F. Toney, S. F. Bent and M. D. McGehee, *Sustain. Energy Fuels*, 2018, **2**, 2450–2459.
77 J. Kim, S. H. Lee, C. H. Chung and K. H. Hong, *Phys. Chem. Chem. Phys.*, 2016, **18**, 4423–4428.
78 G. E. Eperon, S. D. Stranks, C. Menelaou, M. B. Johnston, L. M. Herz and H. J. Snaith, *Energy Environ. Sci.*, 2014, **7**, 982.
79 D.-Y. Son, J.-W. Lee, Y. J. Choi, I.-H. Jang, S. Lee, P. J. Yoo, H. Shin, N. Ahn, M. Choi, D. Kim and N.-G. Park, *Nat. Energy*, 2016, **1**, 16081.
80 M. Saliba, T. Matsui, J. Y. Seo, K. Domanski, J. P. Correa-Baena, M. K. Nazeeruddin, S. M. Zakeeruddin, W. Tress, A. Abate, A. Hagfeldt and M. Gratzel, *Energy Environ. Sci.*, 2016, **9**, 1989–1997.
81 J. H. Noh, S. H. Im, J. H. Heo, T. N. Mandal and S. I. Seok, *Nano Lett.*, 2013, **13**, 1764–1769.
82 Z. Zhang, C. Cueto, Y. Ding, L. Yu, T. P. Russell, T. Emrick and Y. Liu, *ACS Appl. Mater. Interfaces*, 2022, **14**, 29896–29904.
83 G. E. Eperon, T. Leijtens, K. A. Bush, R. Prasanna, T. Green, J. T. Wang, D. P. McMeekin, G. Volonakis, R. L. Milot, R. May, A. Palmstrom, D. J. Slotcavage, R. A. Belisle, J. B. Patel, E. S. Parrott, R. J. Sutton, W. Ma, F. Moghadam, B. Conings, A. Babayigit, H. G. Boyen, S. Bent, F. Giustino, L. M. Herz, M. B. Johnston, M. D. McGehee and H. J. Snaith, *Science*, 2016, **354**, 861–865.
84 R. Wang, M. Mujahid, Y. Duan, Z. K. Wang, J. Xue and Y. Yang, *Adv. Funct. Mater.*, 2019, **29**, 1808843.
85 D. P. McMeekin, S. Mahesh, N. K. Noel, M. T. Klug, J. Lim, J. H. Warby, J. M. Ball, L. M. Herz, M. B. Johnston and H. J. Snaith, *Joule*, 2019, **3**, 387–401.
86 Z. Li, S. Wu, J. Zhang, K. C. Lee, H. Lei, F. Lin, Z. Wang, Z. Zhu and A. K. Y. Jen, *Adv. Energy Mater.*, 2020, **10**, 2000361.
87 X. Li, X. Wu, B. Li, S. Zhang, Y. Liu, Z. Li, D. Zhang, X. Wang, Q. Sun, D. Gao, C. Zhang, W. H. Huang, C. C. Chueh, C. L. Chen, S. Yang, S. Xiao, Z. Wang and Z. Zhu, *ACS Nano*, 2023, **17**, 23478–23487.
88 K. O. Brinkmann, T. Becker, F. Zimmermann, C. Kreusel, T. Gahlmann, M. Theisen, T. Haeger, S. Olthof, C. Tuckmantel, M. Gunster, T. Maschwitz, F. Gobelsmann, C. Koch, D. Hertel, P. Caprioglio, F. Pena-Camargo, L. Perdigon-Toro, A. Al-Ashouri, L. Merten, A. Hinderhofer, L. Gomell, S. Zhang, F. Schreiber, S. Albrecht, K. Meerholz, D. Neher, M. Stolterfoht and T. Riedl, *Nature*, 2022, **604**, 280–286.
89 X. Wu, Y. Liu, F. Qi, F. Lin, H. Fu, K. Jiang, S. Wu, L. Bi, D. Wang, F. Xu, A. K. Y. Jen and Z. Zhu, *J. Mater. Chem. A*, 2021, **9**, 19778–19787.
90 B. Qi and J. Wang, *J. Mater. Chem.*, 2012, **22**, 24315.
91 N. K. Elumalai and A. Uddin, *Energy Environ. Sci.*, 2016, **9**, 391–410.
92 C. Li, Z. Song, C. Chen, C. Xiao, B. Subedi, S. P. Harvey, N. Shrestha, K. K. Subedi, L. Chen, D. Liu, Y. Li, Y.-W. Kim, C.-s. Jiang, M. J. Heben, D. Zhao, R. J. Ellingson, N. J. Podraza, M. Al-Jassim and Y. Yan, *Nat. Energy*, 2020, **5**, 768–776.
93 S. H. Turren-Cruz, A. Hagfeldt and M. Saliba, *Science*, 2018, **362**, 449–453.
94 Z. Jia, X. Guo, X. Yin, M. Sun, J. Qiao, X. Jiang, X. Wang, Y. Wang, Z. Dong, Z. Shi, C. H. Kuan, J. Hu, Q. Zhou, X. Jia, J. Chen, Z. Wei, S. Liu, H. Liang, N. Li, L. K. Lee, R. Guo, S. V. Roth, P. Muller-Buschbaum, X. Hao, X. Du and Y. Hou, *Nature*, 2025, **643**, 104–110.
95 Y. Han, J. Fu, Z. Ren, J. Yu, Q. Liang, Z. Xu, X. Xie, D. Li, R. Ma, M. Cao, Y. Sun, C. Yang, J. He, X. Chang, K. Liu, P. W. K. Fong, J. Huang, H. Liu, Z. Liu, D. Xu, L. Cheng, J. Zhang, G. Yang, X. Lu, Y. Zhu, Q. Tai, Q. Lin, H. Hu, Y. Yang and G. Li, *Nat. Energy*, 2025, **10**, 513–525.
96 S. Jiang, R. Wang, M. Li, R. Yu, F. Wang and Z. a. Tan, *Energy Environ. Sci.*, 2024, **17**, 219–226.
97 Z. He, R. Yu, Y. Dong, R. Wang, Y. Zhang and Z. Tan, *Nat. Commun.*, 2025, **16**, 1773.
98 K. Lang, J. Xu, H. Han, H. Liu, Y. Fu, X. Zhang, Z. Sun, Q. Shi, Z. a. Tan and J. Yao, *Adv. Funct. Mater.*, 2025, **35**, 2502966.
99 Z. Song, J. Wang, Y. Bao, J. Zeng, D. Wang, J. He, P. Zhu, B. Jiang, Z. Liu, S. He, Y. Hou, Z. Hu, C. Xie, Y. Chen, Y. Liu, X. Wang and B. Xu, *Energy Environ. Sci.*, 2025, **18**, 4883–4892.
100 S. Liu, L. Hao, J. Yu, Y. Xu, Y. Dou, J. Xie, Y. Wang, K. Zhang, F. Huang and Y. Cao, *ACS Nano*, 2025, **19**, 748–759.
101 J. G. Son, S. Ameen, J. Roe, S. Park, J. Seo, J. Kim, A. B. Faheem, H. e. Koo, S. O. Oh, Y. Jo, J. W. Kim, Y. Lee, Y. S. Shin, H. Jang, D. Lee, S. Hur, K. K. Lee, S. Cho, D. S. Kim, J. Y. Kim and B. Kim, *Adv. Energy Mater.*, 2025, **15**, 2404092.
102 E. T. Hoke, D. J. Slotcavage, E. R. Dohner, A. R. Bowring, H. I. Karunadasa and M. D. McGehee, *Chem. Sci.*, 2015, **6**, 613–617.
103 S. Wu, M. Liu and A. K. Y. Jen, *Joule*, 2023, **7**, 484–502.
104 X. Meng, X. Liu, Q. Zhou, Z. Liu and W. Chen, *Nano Energy*, 2024, **128**, 109984.
105 H. Hoppe and N. S. Sariciftci, *J. Mater. Res.*, 2011, **19**, 1924–1945.
106 H. Neugebauer, C. Brabec, J. C. Hummelen and N. S. Sariciftci, *Sol. Energy Mater. Sol. Cells*, 2000, **61**, 35–42.
107 S. Gunes, H. Neugebauer and N. S. Sariciftci, *Chem. Rev.*, 2007, **107**, 1324–1338.
108 T. Liu, Q. C. Burlingame, M. R. Ivancevic, X. Liu, J. Hu, B. P. Rand and Y. L. Loo, *Adv. Energy Mater.*, 2023, **13**, 2300046.
109 W. Chen, D. Li, X. Chen, H. Chen, S. Liu, H. Yang, X. Li, Y. Shen, X. Ou, Y. Yang, L. Jiang, Y. Li and Y. Li, *Adv. Funct. Mater.*, 2021, **32**, 2109321.
110 Y. Wang, B. Liu, D. Zhang, H. Yu, X. Wu, D. Gao, B. Li, C. Zhang, W. Liu, Z. Yu, N. Wang, L. Wang, X. Li, H. Yan and Z. Zhu, *Small*, 2025, **21**, e2411031.
111 H. Zhang, Y. Luo, T. A. Dela Peña, R. Ma, H. Yan, M. Li, M. Suryawanshi, J. Wu and A. Uddin, *Adv. Mater. Interfaces*, 2025, **12**, 2500204.

112 Y. Li, Y. Yan, Y. Fu, W. Jiang, M. Liu, M. Chen, X. Huang, G. Lu, X. Lu, J. Yin, S. Wu and A. K. Jen, *Angew. Chem., Int. Ed.*, 2024, **63**, e202412515.

113 J. G. Son, H.-e. Koo, W. Lee, D. Kim, S. Park, J. Roe, J. Seo, J. M. Ha, H. Lee, W. Lee, H. Y. Woo, S. Cho, D. S. Kim, S.-J. Shin and J. Y. Kim, *Energy Environ. Sci.*, 2026, **19**, 1540–1550.

114 X. Chen, Z. Jia, Z. Chen, C. Zhou, S. Huang, X. Xia, S. Liang, P. Wang, T. Jiang, T. Liu, X. Xu, B. Yan, J. Yao, X. Lu, W. Shen, H. Zhu and Y. M. Yang, *Adv. Mater.*, 2025, **37**, e2500190.

115 C. Kan, C. Luo and Y. Hou, *Energy Environ. Sci.*, 2026, **19**, 1101–1123.

116 P. Wu, D. Thrithamarassery Gangadharan, M. I. Saidaminov and H. Tan, *ACS Cent. Sci.*, 2023, **9**, 14–26.

117 B. Taheri, F. De Rossi, G. Lucarelli, L. A. Castriotta, A. Di Carlo, T. M. Brown and F. Brunetti, *ACS Appl. Energy Mater.*, 2021, **4**, 4507–4518.

118 M. Zhang and Z. Lin, *Energy Environ. Sci.*, 2022, **15**, 3152–3170.

119 O. Astakhov, T. Cibaka, L. Wieprecht, U. Rau and T. Merdzhanova, *ChemSusChem*, 2025, **18**, e202402027.

120 S. Baumann, G. E. Eperon, A. Virtuani, Q. Jeangros, D. B. Kern, D. Barrit, J. Schall, W. Nie, G. Oreski, M. Khenkin, C. Ulbrich, R. Peibst, J. S. Stein and M. Köntges, *Energy Environ. Sci.*, 2024, **17**, 7566–7599.

121 D. Kumar, C. Zhang, E. Holubnyak and S. Demirkesen, *Int. J. Hydrogen Energy*, 2024, **95**, 389–401.